

Spontaneous symmetry breaking in a $SO(3)$ non-Abelian lattice gauge theory in $2+1$ D with quantum algorithms

Sandip Maiti ^{1,2,*} Debasish Banerjee ^{1,2,3,†} Bipasha Chakraborty ^{3,‡} and Emilie Huffman ^{4,§}

¹*Saha Institute of Nuclear Physics, HBNI, 1/AF Bidhannagar, Kolkata 700064, India*

²*Homi Bhabha National Institute, Training School Complex, Anushaktinagar, Mumbai 400094, India*

³*School of Physics and Astronomy, University of Southampton, University Road, Southampton, UK*

⁴*Perimeter Institute for Theoretical Physics, Waterloo, ON N2L 2Y5, Canada*

(Dated: July 31, 2025)

The simulation of various properties of quantum field theories is rapidly becoming a testing ground for demonstrating the prowess of quantum algorithms. Some examples include the preparation of ground states, as well as the investigation of various simple wave packets relevant for scattering phenomena. In this paper, we study the ability of quantum algorithms to prepare ground states in a matter-free non-Abelian $SO(3)$ lattice gauge theory in $2+1$ D in a phase where the global charge conjugation symmetry is spontaneously broken. This is challenging for two reasons: the necessity of dealing with a large Hilbert space for gauge theories compared to that of quantum spin models, and the closing of the gap between the two ground states, which becomes exponentially small as a function of the volume. To deal with the large Hilbert space of gauge fields, we demonstrate how the exact imposition of the non-Abelian Gauss Law in the rishon representation of the quantum link operator significantly reduces the degrees of freedom. Further, to resolve the gap, we introduce symmetry-guided ansätze in the Gauss-Law-resolved basis for trial states as the starting point for the quantum algorithms to prepare the two lowest energy states. In addition to simulation results for a range of two-dimensional system sizes, we also provide experimental results from the trapped-ion-based quantum hardware, IonQ, when working on systems with four quantum links. The experimental/simulation results derived from our theoretical developments indicate the role of metrics—such as the energy and the infidelity—to assess the obtained results.

I. INTRODUCTION

The success of quantum field theory (QFT) as a paradigm to explain the properties of physical systems in Nature has proceeded hand in hand with the development of computational techniques in this framework. One of the key advances was the development of renormalized perturbation expansion in quantum field theory [1], allowing the computation of quantities which could be matched with experiments, and culminating in the resounding success of quantum electrodynamics. However, the theory of strong interactions has proven to be a challenge for perturbation theory, since the presence of strong interactions between the quarks and gluons result in non-perturbative phenomena such as confinement. This necessitated the introduction of lattice gauge theory [2, 3], and the Markov Chain Monte Carlo methods for non-perturbative evaluation of physical quantities in QFTs [4, 5].

While there has been considerable improvement in various Monte Carlo techniques, there are domains where the role of Monte Carlo as a superior method from existing methods has not been established. Investigation of matter at finite densities is one prime example, especially in the case of doped Hubbard model (relevant for

high-temperature superconductivity), or quantum chromodynamics (QCD) at finite baryon density (relevant for equation of state of neutron stars). Similarly, studies of the real-time dynamics of QFTs or quantum many body systems can hardly be addressed with Monte Carlo methods. Powerful variational methods [6–8] involving matrix product and tensor network states can address both the above problems in lower dimensions, but it is not clear whether these problems can be addressed fully in thermodynamically large systems.

In this ecosystem, the technological realization of quantum computation, which was theoretically inspired by [9, 10], has ushered in a new array of opportunities for the development of computational paradigms. Hamiltonians of relevant physical systems can be designed by controlling various quantum degrees of freedom (such as ions, atoms, or molecules) in various hardware (ion-traps, optical lattices, superconducting qubits, Rydberg systems) and tuning interactions between them [11–19]. In principle, quantum computation may be used for both of the aforementioned difficult cases of simulations of matter at finite densities and of real-time dynamics, although in reality nontrivial work is necessary to address any physically relevant system. Currently, efforts are underway to design and test quantum algorithms in toy quantum field theories to demonstrate their capabilities of both reproducing and going beyond results obtained through well-known classical methods [20–34]. Simultaneously, there are also efforts in the development of novel theoretical methods and models, which can be seamlessly adapted to the framework of quantum technologies [35–51].

* sandip.maiti@saha.ac.in

† debasish.banerjee@saha.ac.in

‡ B.Chakraborty@soton.ac.uk

§ ehuffman@perimeterinstitute.ca

As advancements in the controllability of noisy intermediate-scale quantum (NISQ) [52] computers have emerged, there is a growing focus on variational quantum simulation (VQS). The main objective of VQS involves using variational algorithms, such as variational quantum eigensolvers (VQEs) [53], to estimate the ground-state spectrum of a quantum Hamiltonian. At the core of VQEs lies the development of parametrized quantum circuits. [54, 55] As an example, a specific VQE variant, utilizing the hardware-efficient ansatz consisting of parametrized single-qubit rotation gate layers and non-parametrized entangling gate blocks, has been employed to address the ground-state energy of a quantum many-body system. An extension of VQE, known as variational quantum deflation (VQD) [56], allows for the computation of excited state spectra by incorporating overlap terms into the optimization function. This procedure comes at almost no extra cost.

In contrast to the VQE utilizing the hardware-efficient ansatz, another well-known type of variational algorithm is the quantum approximate optimization algorithm (QAOA) [57, 58], where the circuit ansatz is referred to as the Hamiltonian variational ansatz, and the design of the quantum circuit is intricately linked to the problem Hamiltonian. It was initially designed for solving combinatorial minimization problems like the Max-Cut problem [59]. As is sometimes expected from large multidimensional variational problems, one can run into barren plateaus. While barren plateaus are present in the optimization landscape of both VQEs using the hardware-efficient ansatz and the QAOA, the QAOA has been developed in part to reduce the probability of encountering such plateaus, and in both cases sometimes minor adaptations in a particular ansatz may eliminate them [60].

In addition to the general simulation issues described above, there are also symmetry-based issues that may arise in studying particular phases of physical systems. Symmetries play a crucial role in modern physics in the context of classifying various phases of matter. The Ginzburg-Landau paradigm [61] of classifying phases and phase transitions has largely governed numerous theoretical and experimental explorations both in classical and quantum physics. Consequently, the idea that symmetries can be spontaneously broken, especially at low temperatures or at finite densities, has facilitated the identification of phases present in systems of physical interest. In fact, the spontaneous breaking of chiral symmetry in quantum chromodynamics (QCD) is responsible for the mass of visible matter (such as protons and neutrons) around us, while the spontaneous breaking of a global $U(1)$ symmetry is responsible for superconductivity in a theory of (weakly-interacting) fermions. Given the importance of spontaneous symmetry breaking (SSB) to physically-relevant systems, it is natural to develop quantum algorithms suited for the preparation of these symmetry-broken ground states. In a given system, the phenomenon of SSB indicates the presence of multiple ground states $|\psi_i\rangle$ (where i labels the different symmetry

broken ground state), which transform into each other by the action of a global symmetry operator U . In the scenario where SSB does not occur, then the ground state is unique, and has even quantum numbers corresponding to all symmetries.

However, the relevant theoretical setup for (classical or quantum) numerical studies is a finite box with a lattice structure, such that both ultraviolet and infrared fluctuations are regulated. In such a finite volume setup, the ground state is not degenerate, but gapped. Moreover, the gap decreases exponentially with increase in the volume. Therefore, it is relevant to ask how would a variational algorithm, especially realized with quantum hardware, fare when asked to prepare the ground state(s) of such a phase. Note that no problems are expected when such a study is undertaken for the ground state of a gapped theory: the separation between the ground state energy E_0 and the first excited state E_1 is typically of the energy scale of theory: $\Delta E \sim J$, where J is the energy scale associated with the Hamiltonian. In contrast, for SSB one has $\Delta E \sim \exp(-cV)$, thus challenging the gap extraction using variational methods (where c is a constant number, and V is the physical volume).

Our primary goal is to address these challenges and demonstrate SSB within a pure gauge theory using variational quantum algorithms. The impracticality of directly implementing the Wilsonian version of the theory (commonly used in classical computation) on a quantum computer arises from the infinite-dimensional Hilbert space associated with each gauge link. One direction to proceed is to truncate the local infinite-dimensional Hilbert space, leading one to deal with breaking of gauge invariance appropriately. A viable alternative is to explore a different framework within gauge theory referred to as quantum link models (QLM) [62], where each gauge link is replaced by a finite-dimensional Hilbert space while preserving the local gauge invariance, and rendering it suitable for quantum computer implementation. Thus, it is possible to ensure that gauge symmetry is preserved throughout the quantum simulation. Abelian formulations have already been extensively explored, and we proceed to non-Abelian gauge theories while treading the road to quantum chromodynamics in the long-term. We concentrate on a theory characterized by local symmetries of $SO(3)$ and investigate its representations across various lattice geometries, including bubble, triangular, and square lattice structures. The model has been previously investigated [63], particularly regarding spontaneous symmetry breaking (SSB) phenomena through the use of exact diagonalization (ED). However, as the computational demands in ED grow exponentially with system volume, exploring significantly larger systems becomes impractical. Additionally, the Monte Carlo method becomes difficult, mainly due to the sign problem within the chosen basis of the Hilbert space. Consequently, it would be beneficial to employ quantum computing to study the model and demonstrate SSB phenomena in larger systems. In illustrating SSB, we employ a range of quantum algorithms to calculate both

the ground state and a subset of excited state spectra.

In this article, we thus propose and benchmark a class of quantum algorithms to extract the low-energy spectrum of a $SO(3)$ non-Abelian lattice gauge theory without matter. Typically, gauge theories have many more degrees of freedom than a corresponding spin or fermionic model, and are thus more resource expensive to simulate on a quantum platform. Moreover, only gauge-invariant degrees of freedom contribute to the dynamics, and thus mapping all degrees of freedom of the original model onto the quantum computer is not very useful. We show that in the quantum link formulation it is possible to impose Gauss' Law analytically, and reformulate the model entirely in terms of gauge-invariant degrees of freedom. The other question which we address in this paper is the efficacy of the various variational quantum algorithms to capture the ground state and the mass gap of the theory, which in turn depends on the global symmetries of the Hamiltonian, and whether they are broken or not.

The rest of the paper is arranged as follows: in Sec. II, we describe the model and its local gauge invariance, and formulate it in a gauge-invariant way; in Sec. III, we provide a comprehensive description of the quantum algorithms used in the investigation of symmetry breaking physics. Sec. IV is dedicated to the discussion of our results: first we discuss the VQE methods on real hardware (before imposing gauge invariance) and display our results; then we discuss our attempts to study SSB phenomena using quantum algorithms on classical hardware, up to 12 qubits. In Sec. V, we compare our results to that obtained for the transverse field Ising model (TFIM) in the SSB phase to demonstrate the difficulty of simulating a full-fledged gauge theory as opposed from a spin model. We conclude our discussion in Sec. VI, summarizing the main results and providing an outlook for the research direction which this work inspires.

II. MODEL, SYMMETRIES, AND GAUGE INVARIANT STATES

Here we discuss the model with a local $SO(3)$ gauge invariance, operators corresponding to microscopic gauge fields, and the appropriate gauge symmetries. Readers familiar with the structure of quantum link models can skip this section, an almost equivalent description is provided in [63]. The basic degrees of freedom are the $SO(3)$ matrix-valued gauge fields: O_{xy}^{ab} (where $a, b \in 1, 2, 3$). Each element of the gauge field is a Hermitian operator $O^{ab\dagger} = O^{ab}$ which lives on the link joining the lattice sites x and $y = x + \mu$. We denote the unit vectors in the positive direction as $+\mu, +\nu, \dots$, while the unit vectors in the negative direction are $-\mu, -\nu, \dots$. This notation is useful since we will define operators which live on the left and right (top and bottom) positions of a link. The canonically conjugate momenta are the matrix-valued left and right electric fields, denoted as $L_{x,+\mu}^a$ and $R_{x+\mu,-\mu}^a$ respectively (also Hermitian), and shown in Fig. 1. The

non-Abelian electric fields at different links always commute with each other. However, for a specified link, while L^a and the R^a commute with each other, $[L^a, R^b] = 0$, the others satisfy the following commutation relations:

$$[L^a, L^b] = 2i\varepsilon^{abc}L^c, \quad [R^a, R^b] = 2i\varepsilon^{abc}R^c, \quad (1)$$

where ε^{abc} is the usual Levi-Civita symbol.

Just like position and momentum operators, the electric and the gauge field operators on the same link satisfy certain commutation relations among themselves (while those associated with different links commute):

$$[L^a, O^{bd}] = 2i\varepsilon^{abc}O^{cd}; \quad [R^a, O^{bd}] = -2iO^{bc}\varepsilon^{acd}, \quad (2)$$

and similarly, due to their non-Abelian nature the different elements of the O^{ab} satisfy the following commutation rules:

$$[O^{ab}, O^{cd}] = 2i\delta^{ac}\varepsilon^{ebd}R^e + 2i\delta^{bd}\varepsilon^{eac}L^e. \quad (3)$$

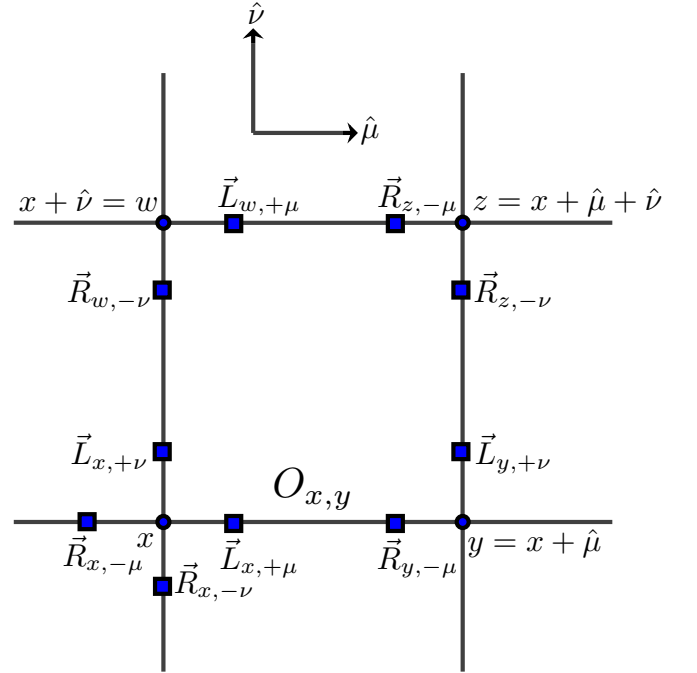


FIG. 1. The plaquette in a two-dimensional spatial lattice. The gauge field operators are denoted as O_{xy}^{ab} where a, b are the color indices and x, y are the ends of the links on which the gauge field is defined. The non-Abelian electric fields are $L_{x,+\mu}^a$ and $R_{y,-\mu}^a$, and are defined on the left and right side of the link joining sites x and y respectively.

Using these operators, we can now construct the Hamiltonian operator. A generic Hamiltonian for a (lattice)

gauge theory has terms containing the electric field energy and the magnetic field energy, $\mathcal{H} = \mathcal{H}_E + \mathcal{H}_B$. In terms of the electric field operators, the first term is $\mathcal{H}_E = \frac{g^2}{2} \sum_{x,\mu} (L_{x,+\mu}^a L_{x,+\mu}^a + R_{x+\mu,-\mu}^a R_{x+\mu,-\mu}^a)$. The magnetic term is the plaquette term, defined as a product of the four oriented links around the smallest square loop on the lattice, $\mathcal{H}_B = -\frac{1}{4g^2} \sum_{\square} \text{Tr} \mathcal{O}_{\square}$, where $\mathcal{O}_{\square}^{ab} = O_{xy}^{am} O_{yz}^{mn} O_{zw}^{np} O_{wx}^{pb}$, and x, y, z, w label the four corners of the plaquette \square starting from bottom left and moving anticlockwise. Since the operator is already Hermitian, the conjugate is unnecessary.

Hamiltonians with this structure are invariant under a larger class of local transformations, often called gauge symmetries. These transformations are generated by the local Gauss Law, which is the non-Abelian analogue of $\nabla \cdot E = 0$,

$$G_x^a = \sum_{\mu} (L_{x,+\mu}^a + R_{x,-\mu}^a), \quad [G^a, G^b] = 2i\epsilon^{abc} G^c, \quad (4)$$

where the various components of the Gauss Law do not commute. Moreover, the electric field operators which appear in the Gauss Law are schematically shown in Fig. 1.

Typically, if one is working in a computational basis diagonal in the electric field, it is non-trivial to form totally gauge invariant states. In this paper we will take a different route: for our chosen operators, we first construct a basis which directly projects to the $\vec{G} = 0$ sector, and then construct the Hamiltonian in this gauge invariant basis. Under a generic gauge transformation $V = \prod_x \exp(i\alpha_x^a G_x^a)$, quantum link operators transform as:

$$O_{xy}^{ab} = (V^\dagger O_{xy} V)^{ab} = [e^{i\alpha_x^m t^m}]^{ac} O_{x,y}^{cd} [e^{-i\alpha_y^p t^p}]^{db}, \quad (5)$$

and $t_{bc}^a = -\epsilon^{abc}$ are the generators of the $SO(3)$ group. A sketch of the operators on the lattice is shown in Fig. 1. The detailed transformation is provided in the Appendix A as a reference.

Representations of field operators: As the next step, we need to choose concrete representations for the operator structures discussed above. There is a simple method to construct such representations following [64, 65]. We first note that in order to represent O^{ab} , we need N^2 Hermitian operators, for each of L^a, R^a , we need N hermitian operators, and thus a total of $N^2 + 2N$ operators. With $N = 3$, this gives 15 hermitian operators, and this can be represented by the 15 elements of the $so(6)$ algebra, linearly independent by construction. The $so(6)$ forms the embedding algebra for this model.

The simplest representation for the operators is to have a spin- $\frac{1}{2}$ bilinear operator to represent the gauge and the electric fluxes as follows:

$$\begin{aligned} O_{xy}^{ab} &= \sigma_{x,+\mu}^a \otimes \sigma_{x+\mu,-\mu}^b, \\ L_{x,+\mu}^a &= \sigma_{x,+\mu}^a \otimes \mathbb{I}, \quad R_{x+\mu,-\mu}^a = \mathbb{I} \otimes \sigma_{x+\mu,-\mu}^a. \end{aligned} \quad (6)$$

Each operator in the bilinear is called a rishon. Note that we have explicitly chosen the smallest representation possible here, the spin- $\frac{1}{2}$, and the generators are then simply the tensor products of the Pauli operators. In general, it is also possible to choose a spin-1, or any other allowed representations. Typically, it is expected that with integer-valued spins one obtains theories whose ground states behave qualitatively similar to that of the corresponding Wilson formulation of the theory [44]. On the other hand, choice of a half-integer spin gives rise to a novel phases, often relevant in the context of non-trivial θ -terms [66, 67].

This representation was also the subject of [63], where the physics in $(1+1)$ -d dimension was studied in the presence of dynamical fermionic fields. In this article, we extend the studies to two spatial dimensions, and inclusion of fermions in the two-dimensional model is underway. A key feature of the spin- $\frac{1}{2}$ representation is that the electric field energy term does not explicitly appear in the Hamiltonian, since both the fields square to yield a constant. However, the fields still remain dynamical, influencing the theory by choosing the physical Hilbert space through the Gauss' Law. The magnetic field is fully non-trivial, and in terms of the chosen operators we have:

$$\begin{aligned} \text{Tr} \mathcal{O}_{\square} &= (\sigma_{x,+\mu}^a \otimes \sigma_{y,-\mu}^b) \otimes (\sigma_{y,+\nu}^b \otimes \sigma_{z,-\nu}^c) \\ &\otimes (\sigma_{z,-\mu}^c \otimes \sigma_{w,+\mu}^d) \otimes (\sigma_{w,-\nu}^d \otimes \sigma_{x,+\nu}^a). \end{aligned} \quad (7)$$

The location of the operators are shown in Fig. 1, and the trace on the left-hand side is implemented on color indices, as can be seen explicitly in the above equation. The local plaquette is clearly a 256-dimensional matrix.

Gauss Law: A general gauge transformation is given by $V = \prod_x \exp(-i\alpha_x^a G_x^a)$. Using equation (7), the Gauss Law (in the absence of any matter field) is

$$G_x^a = \sum_{\mu} \left(\sigma_{x,+\mu}^a + \sigma_{x,-\mu}^a \right). \quad (8)$$

Demanding a physical state to be gauge-invariant is equivalent to selecting states according to the condition $G_x^a |\psi\rangle = 0$.

Construction of gauge-invariant states: Now, we discuss the construction of singlet states under gauge transformations in both one and two spatial dimensions. These states are sometimes called *glueball* states [65]. In one spatial dimension, there are two links touching a site x , and a gauge invariant state can be easily constructed as follows:

$$\begin{aligned} |\psi_s\rangle_{x,+\mu,-\mu} &= \frac{1}{\sqrt{2}} \left(|\uparrow\rangle_{x,+\mu} |\downarrow\rangle_{x,-\mu} - |\downarrow\rangle_{x,+\mu} |\uparrow\rangle_{x,-\mu} \right). \end{aligned} \quad (9)$$

The state $|\psi_s\rangle_x$ is gauge-invariant, which means $G_x^3 |\psi_s\rangle_x = 0$, $G_x^+ |\psi_s\rangle_x = 0$, and $G_x^- |\psi_s\rangle_x = 0$, where the

operators G_x^+ and G_x^- are defined as $G^+ = \frac{1}{\sqrt{2}}(G^1 + iG^2)$, $G^- = \frac{1}{\sqrt{2}}(G^1 - iG^2)$ respectively. We can construct a triplet state at site x as follows

$$\begin{aligned} |\psi_1\rangle_{x,+\mu,-\mu} &= |\uparrow\rangle_{x,+\mu} |\uparrow\rangle_{x,-\mu} \\ |\psi_2\rangle_{x,+\mu,-\mu} &= \frac{1}{\sqrt{2}} \left(|\uparrow\rangle_{x,+\mu} |\downarrow\rangle_{x,-\mu} \right. \\ &\quad \left. + |\downarrow\rangle_{x,+\mu} |\uparrow\rangle_{x,-\mu} \right) \\ |\psi_3\rangle_{x,+\mu,-\mu} &= |\downarrow\rangle_{x,+\mu} |\downarrow\rangle_{x,-\mu}. \end{aligned} \quad (10)$$

The triplet states represent external static charges and are useful to track the total number of allowed states with the chosen representation.

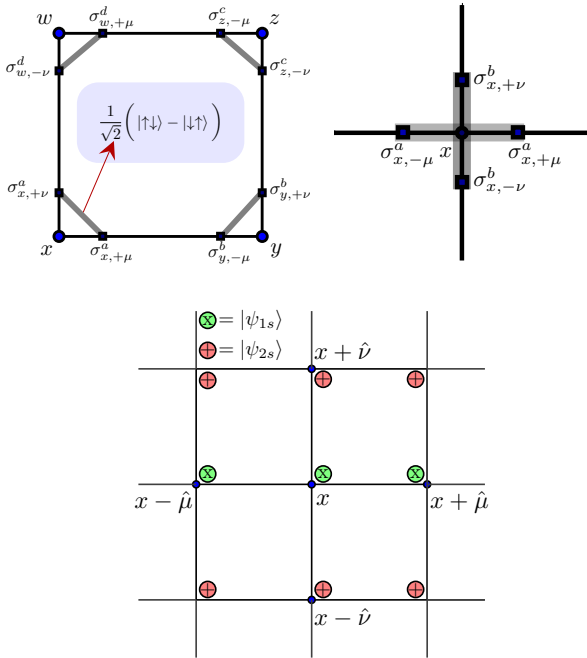


FIG. 2. (Top left): Gauge-invariant states for the plaquette can be constructed by creating singlets of each pair of spins at the corners. The figure illustrates how the singlets are constructed at each corner. (Top right): The location of the four spins relative to a lattice site, which is used in the construction of gauge-invariant states for a 2D lattice. Four spin- $\frac{1}{2}$ are considered, and as explained in the text, two singlets can be constructed. (Bottom): The figure shows one of the states contributing to the ground state, labeled as $|0011\rangle$, on a 2×2 lattice with periodic boundary conditions (PBC) where $|0\rangle$ represents $|\psi_{1s}\rangle$ and $|1\rangle$ represents $|\psi_{2s}\rangle$.

Next in complexity, consider a single plaquette state. In this case also, there are two links touching a site, but in orthogonal directions. As before, we can build four singlet states using two spins touching each corner. Labelling the corner sites as x, y, z, w , the single gauge-invariant state

in this case can be represented as

$$\begin{aligned} |\psi_s\rangle_{\square} &= |\psi_s\rangle_{x,+\mu,+\nu} |\psi_s\rangle_{y,-\mu,+\nu} \\ &\quad |\psi_s\rangle_{z,-\mu,-\nu} |\psi_s\rangle_{w,+\mu,-\nu}. \end{aligned} \quad (11)$$

Since each singlet state is gauge-invariant separately, the state $|\psi_s\rangle_{\square}$ is also gauge-invariant trivially. Further, it is trivial to compute the ground state energy for this state. Noting that each singlet contributes $-\frac{3}{4}$, while there is an additional factor of 2^8 for defining the Hamiltonian via the Pauli $\vec{\sigma}$, instead of the usual \vec{S} operators. This normalization is better suited to studies of the model on quantum computers. The ground state energy for the state $|\psi_s\rangle_{\square}$ is thus

$$\mathcal{H} |\psi_s\rangle_{\square} = -\frac{256}{4g^2} \left(-\frac{3}{4}\right)^4 |\psi_s\rangle_{\square} = -\frac{81}{4g^2} |\psi_s\rangle_{\square}.$$

Let us give an example of how to track the total number of states separately in different Gauss' Law sectors. Because every link operator consists of two spin- $\frac{1}{2}$ s, there are four possible states for each link, so a square plaquette has a total of $4^4 (= 256)$ possible states. As we argued before, only the one such state remains invariant under gauge transformation, which corresponds to the tensor product of pairwise singlets as in Eq. (10). The other states correspond to different charge insertions on the lattice sites. We can decompose the 256 states into different gauge sectors as

$$256 = 1 \oplus 12 \oplus 54 \oplus 108 \oplus 81, \quad (12)$$

where the 1 is the full gauge invariant state (singlets at all corners), and 81 is the number of states at each sites with triplet charges $3^4 = 81$. With a single triplet charge on any lattice site, one has ${}^4C_1 \cdot 3 = 12$ states, and with three triplet charges, one obtains ${}^4C_3 \cdot 3^3 = 108$ states, and finally the 54 corresponds to the situation when any two of the sites have triplet charges.

Gauge-invariant states for four spins: Once the pattern of building singlets to impose the Gauss Law is understood, it is straightforward to push the construction for a large lattice in higher dimensions. We restrict to two space-dimensional plaquettes in this article. For a square lattice, there are four links which touch a single site, and we need to count how many singlets can be constructed with four spin- $\frac{1}{2}$ s. Clearly, since two spin- $\frac{1}{2}$ s give a singlet and a triplet, $1 \oplus 3$, with four spin- $\frac{1}{2}$ s, we get $(1 \oplus 3) \otimes (1 \oplus 3) = 2 \cdot 1 \oplus 3 \cdot 3 \oplus 5$, which means that there are two singlets, three triplets and a single quintet, giving a total of 16 states, as expected.

Consider two spin singlet states at site x given by

$$|\psi_s\rangle_{x,+\mu,-\mu}, |\psi_s\rangle_{x,+\nu,-\nu}. \quad (13)$$

These two states correspond to four spins, and we can create gauge-invariant singlet states for the four spins in

two ways. The first one is given by

$$|\psi_{1s}\rangle_x = |\psi_s\rangle_{x,+\mu,-\mu} \otimes |\psi_s\rangle_{x,+\nu,-\nu}. \quad (14)$$

Using Eq. (12) by combining two triplets, we can construct another gauge-invariant spin singlet state at site x with the linear combination

$$\begin{aligned} |\psi_{2s}\rangle_x &= a |\psi_{1s}\rangle_{x,+\mu,-\mu} |\psi_{3s}\rangle_{x,+\nu,-\nu} \\ &+ b |\psi_{2s}\rangle_{x,+\mu,-\mu} |\psi_{2s}\rangle_{x,+\nu,-\nu} \\ &+ a |\psi_{3s}\rangle_{x,+\mu,-\mu} |\psi_{1s}\rangle_{x,+\nu,-\nu}. \end{aligned} \quad (15)$$

We find the constants $a = -\frac{1}{\sqrt{3}}$ and $b = \frac{1}{2\sqrt{3}}$ by demanding the state $|\psi_{2s}\rangle$ to be normalized and annihilated by G_x^+ or G_x^- .

It is then possible to use a reduced Hilbert space to study the gauge invariant sector that consists of the two singlet states per site, $|\psi_{1s}\rangle_x$ and $|\psi_{2s}\rangle_x$. The Hamiltonian can be expressed in a gauge-invariant way as follows (see Fig. 2 for the site indices, and Appendix B for a derivation of the same):

$$\begin{aligned} H_{\text{inv}} &= -\frac{1}{4g^2} \prod_{i=x,z} \left(\frac{1}{4} (\tau_i^3 - \mathbb{1}_i) + \frac{\sqrt{3}}{4} \tau_i^1 \right) \\ &\times \prod_{i=y,w} \left(\frac{1}{4} (\tau_i^3 - \mathbb{1}_i) - \frac{\sqrt{3}}{4} \tau_i^1 \right). \end{aligned} \quad (16)$$

In moving to the gauge-invariant basis we have reduced our Hilbert space to 2 states per site rather than 4 states per link. In addition, for clarity, we have used the $\vec{\tau}$ operators to describe the action of the Hamiltonian within the two-dimensional gauge-invariant Hilbert space spanned by $|\psi_{1s}\rangle$ and $|\psi_{2s}\rangle$. Thus, for a general 2D lattice with extent $L_x \times L_y$, instead of $4^{2 \cdot L_x \cdot L_y}$, one has to work with $2^{L_x \cdot L_y}$ states. In terms of actual numbers, for the 2×2 system, one can get away by diagonalizing a 16×16 matrix instead of a 65536×65536 one. In actual calculations, we have always used the normalization $\frac{1}{4g^2} = 1$.

Note that G_x^z is zero on these states by construction. The generator for gauge transformations used in this case can be expressed as:

$$G_x^a = \sigma_{x,+\mu}^a + \sigma_{x,-\mu}^a + \sigma_{x,+\nu}^a + \sigma_{x,-\nu}^a, \quad (17)$$

where $a = +, -, z$ correspond to the three Gauss' Laws. A visual representation of this is presented in Fig. 2.

It turns out that the ground state of this model breaks the lattice translation symmetry by a single lattice spacing spontaneously, which is actually identified with charge conjugation [63]. This definition of charge conjugation ensures a smooth integration with staggered fermions, which we are addressing in a future work. The physical translation operator is equivalent to two lattice spacings. From exact diagonalization (ED), the lowest energy gap exponentially decreases with volume, as $\Delta E \sim \exp(-\alpha V)$. This is the telltale signature of discrete symmetry break-

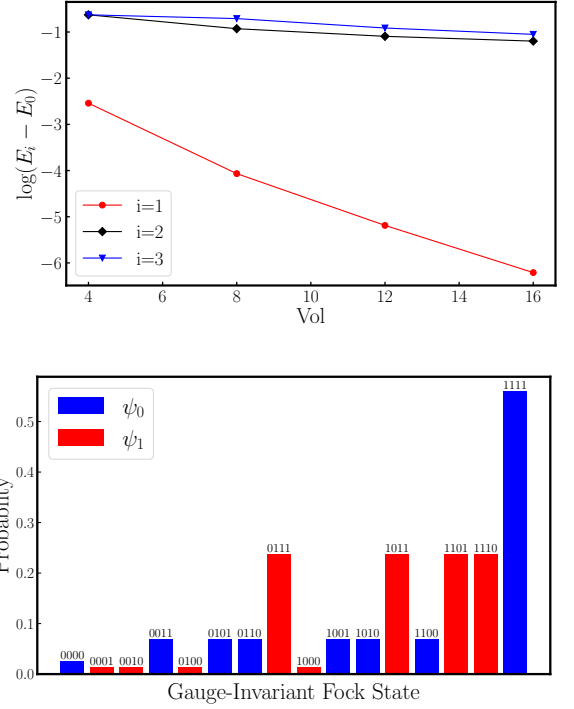


FIG. 3. (Top): Plot of the energy difference within the pure $SO(3)$ QLM in $(2+1)$ -d. If a discrete symmetry breaks spontaneously, the smallest mass gap becomes exponentially small with increase in volume. However, higher energy gaps are insensitive to this. The ED results are consistent with this hypothesis. (Bottom): The probabilities from the wavefunction for the ground state (blue) and first excited state (red) for the 2×2 ($\text{Vol}=4$) system expressed in the gauge invariant basis.

ing in a finite volume, given that the ground state has $C = +1$, while the first excited state has $C = -1$, where C represents the charge conjugation quantum number. This behaviour is illustrated in Fig. 3 (top panel), where the energy difference between the ground state and the first excited state becomes exponentially smaller as a function of volume. But the higher energy gaps ($E_2 - E_0$ and $E_3 - E_0$) are insensitive to the volume. The bottom panel of Fig. 3 shows the ground state and the first excited state wavefunctions, where the symmetry breaking is evident.

III. METHOD

In this section, we describe quantum algorithms to target the low-lying energy states on quantum computers. Since most of the quantum algorithms for this purpose use variational methods, our results indicate how robustly the exponentially small gap in an SSB phase can be extracted using quantum algorithms.

A. Variational Quantum Algorithms

It is well-known from basic quantum mechanics that for a given system described by a quantum Hamiltonian (H), we can estimate the ground state using variational principles. This is directly used in the variational quantum eigensolver (VQE) algorithm, where the following cost function is minimized with respect to the different parameters represented by $\vec{\theta} = \{\theta_1, \dots, \theta_N\}$ (assuming N variational parameters):

$$E(\vec{\theta}) = \langle \psi(\vec{\theta}) | H | \psi(\vec{\theta}) \rangle, \quad (18)$$

where $\psi(\vec{\theta})$ is a parameterized ansatz for the real parameters $\vec{\theta}$. Finding the ground state energy of H is equivalent to minimizing the cost function, $E(\vec{\theta})$. Additionally, we can compute the excited state energies using a variational algorithm known as the variational quantum deflation (VQD) algorithm [56], which is an extension of the VQE algorithm. The primary idea is to iteratively remove the influence of the previously found states from the Hamiltonian to find higher excited states. In VQD, the cost function often involves terms that ensure orthogonality to previously found states to prevent overlap. To find the k -th excited state we minimize the cost function:

$$\begin{aligned} F(\vec{\theta}_k) &= \langle \psi(\vec{\theta}_k) | H | \psi(\vec{\theta}_k) \rangle + \sum_{i=0}^{k-1} \beta_i |\langle \psi(\vec{\theta}_k) | \psi(\vec{\theta}_i) \rangle|^2 \\ &= E(\vec{\theta}_k) + \sum_{i=0}^{k-1} \beta_i |\langle \psi(\vec{\theta}_k) | \psi(\vec{\theta}_i) \rangle|^2, \end{aligned} \quad (19)$$

where the first term can be calculated using the same method as VQE, while the second part acts as a penalty, ensuring that the current state is orthogonal to all the previously optimized ones. In practice, the ansatz state $|\psi(\vec{\theta}_k)\rangle$ may not be perfectly orthogonal to the previously found states $|\psi_0\rangle, |\psi_1\rangle, \dots, |\psi_{k-1}\rangle$ during the optimization process. The penalty terms help the optimization to enforce orthogonality. For example, if we already found the ground state $|\psi_0\rangle$ and the first excited state $|\psi_1\rangle$, the cost function for the second excited state $|\psi_2\rangle$ would look like:

$$\begin{aligned} F(\theta) &= \langle \psi_2(\vec{\theta}) | H | \psi_2(\vec{\theta}) \rangle + \beta_0 |\langle \psi_2(\theta) | \psi_0 \rangle|^2 \\ &\quad + \beta_1 |\langle \psi_2(\theta) | \psi_1 \rangle|^2, \end{aligned} \quad (20)$$

where β_0 and β_1 are penalty coefficients, and $|\langle \psi_2(\vec{\theta}) | \psi_0 \rangle|^2$ and $|\langle \psi_2(\vec{\theta}) | \psi_1 \rangle|^2$ represent the overlaps of $|\psi_2(\vec{\theta})\rangle$ with $|\psi_0\rangle$ and $|\psi_1\rangle$ respectively. During optimization, the penalty terms $\beta_0 |\langle \psi_2(\vec{\theta}) | \psi_0 \rangle|^2$ and $\beta_1 |\langle \psi_2(\vec{\theta}) | \psi_1 \rangle|^2$ penalize overlaps with the states with lower energy. If $|\psi_2(\vec{\theta})\rangle$ has a non-zero overlap with $|\psi_0\rangle$ or $|\psi_1\rangle$, these

terms increase the cost function value, discouraging the optimizer from selecting parameters that result in such overlaps.

Even though we want to find a state that is orthogonal to the previously found states, achieving perfect orthogonality through the optimization process can be difficult due to the circuit complexity and the higher dimensional parameter space. The penalty terms provide an effective way to ensure the ansatz state becomes orthogonal by the end of the optimization process. As the optimization progresses, the penalty terms actively reduce any overlap with previously found states. The choice of β_i depends on the specific system and ansatz used. For example, if β_i values are too high, the optimization process will prioritize orthogonality over minimizing the energy. This can lead to a state that is highly orthogonal to previous states but may not represent the true k -th excited state in terms of energy. Conversely, if β_i values are too low, the optimization might not sufficiently enforce orthogonality, leading to an overlap with lower energy states, which could result in an incorrect excited state. These coefficients balance the cost function between lowering the energy and keeping the new state orthogonal to previously found states. In the particular case of the $SO(3)$ model, we start with small values of β , and increase it while keeping track of the dependence of converged energy E_1 with β . An optimal value is chosen from the plateau where E_1 is stable. For the 2×2 lattice, this is $\beta = 1$, and for 2×4 lattice, we chose $\beta = 5$.

There are several options for choosing the initial variational states. For our calculations, we used the variational ansatz with linear connectivity. The basic structure in each layer consists of a sequence of qubits, connected to each other with 2-qubit CNOT gates, and have rotation gates in the Y and Z spin components. The full circuit has several layers of such gates to increase its expressivity. Mathematically, this can be written as:

$$\begin{aligned} |\psi(\theta)\rangle &= \prod_{l=1}^{N_l} \left(\prod_x \exp(-i(\theta'_{l,x}/2)Q_x^3) \prod_x \exp(-i(\theta_{l,x}/2)Q_x^2) \right. \\ &\quad \left. \prod_x \exp(i\pi/4(I_x - Q_x^3) \otimes (I_{x+1} - Q_{x+1}^1)) \right) \\ &\quad \prod_x \exp(-i(\theta'_{0,x}/2)Q_x^3) \prod_x \exp(-i(\theta_{0,x}/2)Q_x^2) |0\rangle. \end{aligned} \quad (21)$$

Fig. 4 illustrates one such ansatz for seven qubits, and for two layers $N_l = 2$. Note that we have called the qubit degrees of freedom to be generically Q^i . In the electric flux basis, they are the same operators as σ^i , while in the gauge invariant basis they are represented through τ^i .

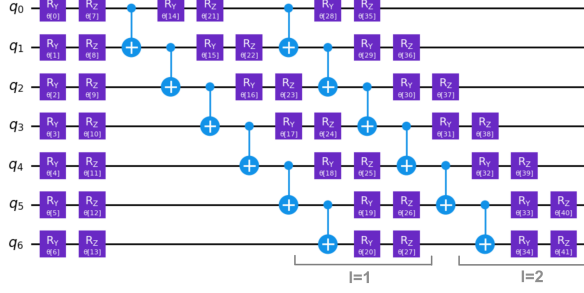


FIG. 4. The variational ansatz for seven qubits and two layers, which alternates two-qubit CNOT gates with single-qubit rotational gates in each layer.

B. Quantum Adiabatic Algorithm and the QAOA

As mentioned in the introduction, the QAOA [59, 68, 69] is a variational quantum algorithm which exploits the form of the quantum Hamiltonian as well as the quantum adiabatic theorem in order to approximate the ground state of the Hamiltonian. According to the quantum adiabatic theorem, if one starts from the ground state of a (simple) Hamiltonian, and adds a coupling which varies with time, then the final state will be (arbitrarily) close to the eigenstate of the final Hamiltonian, provided the variation is done slowly, and assuming non-degenerate initial and the final states [70]. Using this idea, to use the QAOA algorithm, the Hamiltonian is divided into N_α Trotter-inspired parts, H_α , such that

$$H = \sum_{\alpha=1}^{N_\alpha} H_\alpha, \quad (22)$$

where each H_α consists of a sum of terms that commute with one another. This facilitates the choice of an initial state which is the ground state of the starting Hamiltonian.

Then the QAOA ansatz is of the form

$$|GS\rangle_{\text{QAOA}} = \prod_{k=1}^p \prod_{\alpha=1}^{N_\alpha} e^{iC_{\alpha,k}H_\alpha} |\psi_A\rangle, \quad (23)$$

where $|\psi_A\rangle = |\psi_0\rangle$ is the ground state of a portion of the Hamiltonian, which (without loss of generality) we set to be the first term in the sum, $H_{\alpha=1}$. In the limit of infinite layers, there will be a set of $C_{\alpha,k}$ variational parameters that yield the ground state. QAOA as an algorithm works by approximating the ground state for a finite number of parameters, and we can make the ansatz more expressive by increasing p , the number of QAOA layers.

For the $SO(3)$ model in particular, when we break down the Hamiltonian into separate parts, we do so such that one of these terms is a magnetic field in the z -direction, which we set to be our $H_{\alpha=1}$ due to its trivial ground state (note that since the gauge invariant basis is used

here, we use the τ^i operators):

$$H_{\alpha=1} = J \sum_x \tau_x^3, \quad |\psi_{A=0}\rangle = |\uparrow\uparrow \dots \uparrow\rangle. \quad (24)$$

For the 2×2 lattice, the Hamiltonian given by Eq. (16) consists of four spins, and after expanding, we divide it into nine pieces for QAOA:

$$\begin{aligned} H_1 &= \frac{1}{4^3} \sum_{x=1}^4 \tau_x^3, \\ H_2 &= -\frac{1}{4^3} \sum_{x \neq y} \tau_x^3 \tau_y^3 + \frac{1}{4^3} \sum_{x \neq y \neq z} \tau_x^3 \tau_y^3 \tau_z^3 \\ &\quad - \frac{1}{4^3} \tau_1^3 \tau_2^3 \tau_3^3 \tau_4^3, \\ H_3 &= -\frac{3}{4^3} \tau_1^1 \tau_2^1 (-\tau_3^3 \tau_4^3 + \tau_3^3 + \tau_4^3 - I), \\ H_4 &= -\frac{3}{4^3} \tau_3^1 \tau_4^1 (-\tau_1^3 \tau_2^3 + \tau_1^3 + \tau_2^3 - I), \\ H_5 &= -\frac{3}{4^3} \tau_2^1 \tau_3^1 (\tau_1^3 \tau_4^3 - \tau_1^3 - \tau_4^3 + I), \\ H_6 &= -\frac{3}{4^3} \tau_1^1 \tau_3^1 (-\tau_2^3 \tau_4^3 + \tau_2^3 + \tau_4^3 - I), \\ H_7 &= -\frac{3}{4^3} \tau_2^1 \tau_4^1 (-\tau_1^3 \tau_3^3 + \tau_1^3 + \tau_3^3 - I), \\ H_8 &= -\frac{3}{4^3} \tau_1^1 \tau_4^1 (\tau_2^3 \tau_3^3 - \tau_2^3 - \tau_3^3 + I), \\ H_9 &= -\frac{3^2}{4^3} \tau_1^1 \tau_2^1 \tau_3^1 \tau_4^1. \end{aligned} \quad (25)$$

Note that in the typical spin-models considered in the literature, the use of the QAOA form would require at most a few terms in the Hamiltonian. The additional complexity in our case is due to non-Abelian nature of the gauge theory under consideration. The decomposition of Hamiltonian for the 2×4 lattice can be found in the Appendix C. The periodic boundary conditions on ladder systems give rise to more cancellations than are possible for a square geometry. The key point in all of these decompositions is the presence of a term H_1 of the form $H_1 = \sum_{x=1}^N \tau_x^3$.

In order to approximate the first excited state, we use a QAOA-inspired ansatz that makes use of symmetry to ensure it is orthogonal to the ground state (which is then in a different symmetry sector). In analogy to $|\psi_0\rangle$, we define $|\psi_A\rangle$ as

$$|\psi_{A=1}\rangle = |\uparrow\uparrow \dots \downarrow\rangle, \quad (26)$$

where we have flipped the last spin. This state is the one of the degenerate first excited states $|\psi_1\rangle_i = \tau_i^x |\psi_0\rangle$ of $H_{\alpha=1}$, and because the Hamiltonian only flips an even number of spins at a time, it is impossible to get to the ground state by adiabatic evolution. We thus use this state to approximate the first excited state. In fact, Eq. (24) and Eq. (26) are not the only possible initial

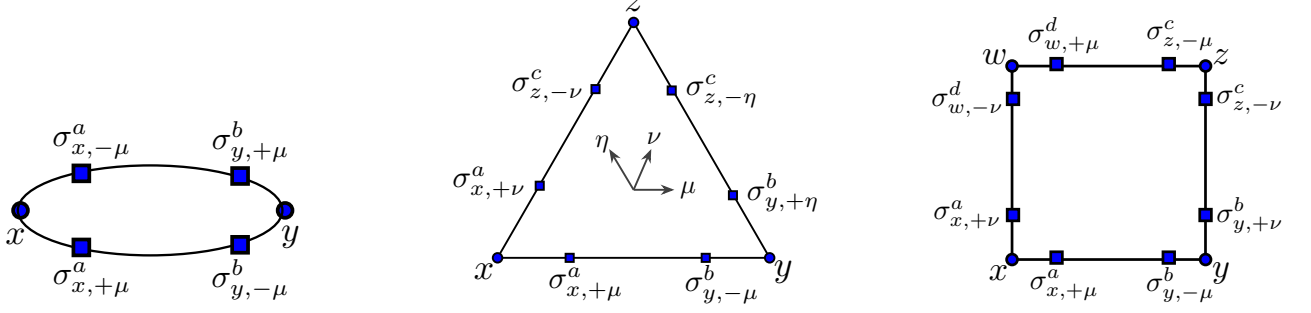


FIG. 5. (Left): A plaquette with two links, the bubble. (Middle): A plaquette with three links, the triangle. (Right): A plaquette with four links, the square.

states for the ground and first excited states. If we start with any state from the same symmetry sector as an initial state, the final state after optimization will always stay in that sector. Moreover, in terms of circuit depth and convergence, the optimization with different initial states is comparable.

IV. RESULTS FOR THE $SO(3)$ QLM

We have applied the different quantum algorithms described in Section III on the pure gauge $SO(3)$ model as described in Section II. We have used both classical and quantum hardware platforms in order to benchmark the performance of the algorithms. The quantum hardware of choice was the trapped-ion quantum computer, IonQ. With the resources available to us, we have been able to study the problem on a small quantum hardware of four qubits. The classical simulation results are for systems with up to 12 qubits.

A. Simple VQE Ansätze with Real Hardware

First, we explore how effective the quantum algorithms perform on NISQ hardware to find the ground state, when working in the gauge field basis where gauge invariance is not imposed. The results can then be compared with exact solutions. We consider three simple systems: the *bubble* plaquette (consisting of two links), the *triangular* plaquette (consisting of three links), and the *square* plaquette (consisting of four links). The IonQ quantum hardware was used to obtain the results only in the first case, the bubble plaquette.

Bubble plaquette: Consider the simplest system first, the bubble plaquette, composed of only two links (Fig. 5, left). From the expression for the link from Eq. (6), we obtain

$$\mathcal{O}_{xy}^{ab} = \sigma_{x,+\mu}^a \otimes \sigma_{y,-\mu}^b, \quad (27)$$

and the Hamiltonian for the bubble plaquette is then given by

$$\mathcal{H}_{\text{bub}} = -J(\sigma_{x,+\mu}^a \sigma_{y,-\mu}^b)(\sigma_{y,+\mu}^b \sigma_{x,-\mu}^a). \quad (28)$$

The two links are physically distinct, and so the operators do not act on the same point. A pictorial representation of this is presented in Fig. 5 (left), where the blue squares indicate the rishon sites. In the spin $S = \frac{1}{2}$ representation (we use Pauli matrices at the expense of a factor of 2), there are two spin halves on each of the two rishon sites on a link, and therefore naively each link has four states. Moreover, the use of the σ^i operators make it clear that we are in the electric flux basis, which is not explicitly gauge invariant.

The analytic argument to obtain gauge singlets is simple: each lattice site connects two rishon sites, one to the immediate left and the other to the immediate right. The two spins on the rishon sites can form a spin singlet, and a spin triplet. The spin-triplet transforms as a charged operator under the Gauss law and thus lies in a high-energy manifold. This is true for both the lattice sites. The total gauge-invariant state for the bubble plaquette is then obtained by a tensor product of the two singlets, one situated at site x and the other at site y . Mathematically, the gauge-invariant ground state can be represented as:

$$|\psi_s\rangle_{\text{bub}} = |\psi_s\rangle_x \otimes |\psi_s\rangle_y, \quad (29)$$

where $|\psi_s\rangle_x$ is the singlet state formed at site x as defined in Eq. (9). The energy for the bubble plaquette is the product of the energy of two independent singlets,

$$\mathcal{H}_{\text{bub}} |\psi_s\rangle_{\text{bub}} = -J(-3)^2 |\psi_s\rangle_{\text{bub}} = -9J |\psi_s\rangle_{\text{bub}}. \quad (30)$$

The VQE used to optimize the parameters of the ansatz is defined as:

$$|\psi(\theta)\rangle_{\text{bub}} = \text{CNOT}_{01} \cdot R_z(\theta)_0 \cdot H_0 \\ \times \text{CNOT}_{23} \cdot R_z(\theta)_2 \cdot H_2 |0101\rangle, \quad (31)$$

where $i = 0, 1, 2, 3$ denote the sites $(x, +\mu)$, $(x, -\mu)$, $(y, -\mu)$, and $(y, +\mu)$ respectively and H_i are the Hadamard operators acting on qubit i .

A single layer of quantum gates with a single variational parameter is sufficient for this example, which is optimized by running the VQE algorithm on an exact quantum simulator. This gives the optimal value of $\theta = \pi$, and the corresponding optimized energy (shown on the right of Fig. 6) converges to the exact value of -9.0 (as given by Eq. (30)) very rapidly. The optimized wavefunction is obtained by using $\theta = \pi$ in Eq. (31) and consists of four Fock states, which can be written as (up to an overall phase)

$$|\psi\rangle_{\text{GI}} = \frac{1}{2}(|1010\rangle - |0110\rangle - |1001\rangle + |0101\rangle). \quad (32)$$

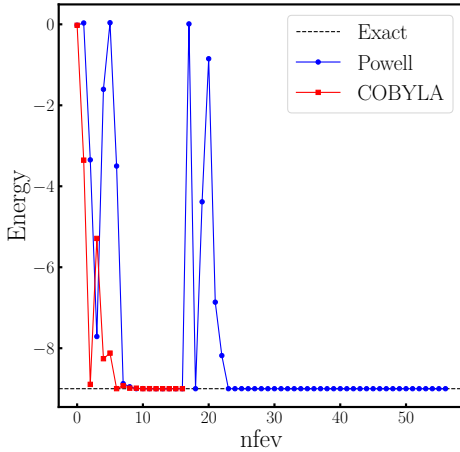


FIG. 6. The convergence of the energy with the number of function evaluations (denoted as nfev on the x-axis) using the classical simulator for two different classical optimizers. In most cases, the COBYLA optimizer performs significantly better than the Powell one.

Triangular and square plaquettes: The calculations done for the triangular and the square plaquettes (with three and four links respectively) are very similar to that of the bubble plaquette. The geometry is illustrated in (Fig. 5 (middle and right) respectively, where the rishon sites are also indicated). The Hamiltonians for

For this example, results using IonQ hardware to obtain the ground state, as shown in Fig. 7. The left subplot shows the energy at each step of the optimization process, while the middle one shows the estimate of the variational parameter, and the right panel plots the fidelity. The fidelity, defined as the overlap between two wavefunctions is commonly used figure-of-merit to judge their equivalence, and is mathematically defined as $f = |\langle\psi_0|\psi_1\rangle|^2$. The ground state energy found by the real hardware is around -8.0 , significantly larger than the exact ground state energy of -9.0 , even though the optimizer for the wavefunction reaches the correct optimal value, $\theta = \pi$. Fig. 7 shows that the energy estimates stabilize after about the first third of the plotted optimization steps. We have put a mark at the 28th step to note the apparent equilibration of results and use the wavefunction obtained at this step to compare with the exact wavefunction. It is important to note that the optimizer is unaware of the gauge invariance of the ground state. The noisy hardware generates spurious states, instead of only the four states expected from Eq. (32). Table I lists the proportions of all the states obtained using the quantum hardware at the 28th step of the optimization and compares them with the exact classical result. While we do see the expected four states that form the gauge-invariant ground state wavefunction dominating (each with probability approximately ~ 0.25), there are 11 other states with probabilities two orders of magnitude smaller than the dominant states. These states will contribute to the wave-function generated by the hardware and will raise the measured energy to -8.1318 instead of -9 . Note that we only have direct access to the measured probabilities of the experimental wave function, and not to the relative signs of the basis states. However, since the optimization of θ parameter of 3.203 is much closer to the analytic value π (the energy deviation is about $\sim 10\%$ while the parameter deviation is about $\sim 2\%$), the fidelity between the ansatz wave function at each variational step is much closer to the analytical answer. This is precisely because the construction of the wave function is gauge-invariant (making singlets at each site) and thus the fidelity calculation (shown in Fig. 7 right) is significantly less contaminated by the gauge non-invariant states than the energy.

the two systems are:

$$\mathcal{H}_{\text{tri}} = -J \text{Tr}(\mathcal{O}_{\Delta}) \\ = -J(\sigma_{x,+\mu}^a \sigma_{y,-\mu}^b)(\sigma_{y,+\eta}^b \sigma_{z,-\eta}^c) \\ (\sigma_{z,-\nu}^c \sigma_{x,+\nu}^a), \quad (33)$$

$$\mathcal{H}_{\text{plaq}} = -J \text{Tr}(\mathcal{O}_{\square}) \\ = -J(\sigma_{x,+\mu}^a \sigma_{y,-\mu}^b)(\sigma_{y,+\nu}^b \sigma_{z,-\nu}^c) \\ (\sigma_{z,-\mu}^c \sigma_{w,+\mu}^d)(\sigma_{w,-\nu}^d \sigma_{x,+\nu}^a). \quad (34)$$

States	Probabilities from exact States	Probabilities from classical simulator	Probabilities from IonQ hardware
0000	0.0	0.0	0.0
0001	0.0	0.0	0.0064
0010	0.0	0.0	0.0061
0011	0.0	0.0	0.0002
0100	0.0	0.0	0.0082
0101	0.25	0.25	0.2436
0110	0.25	0.25	0.2386
0111	0.0	0.0	0.0066
1000	0.0	0.0	0.0048
1001	0.25	0.25	0.2364
1010	0.25	0.25	0.2303
1011	0.0	0.0	0.0061
1100	0.0	0.0	0.0004
1101	0.0	0.0	0.005
1110	0.0	0.0	0.003
1111	0.0	0.0	0.0002

TABLE I. Comparison of results between the exact state, classical simulator, and the quantum hardware for the bubble plaquette. While the classical simulator gives exact zeroes for the probabilities of 12 out of the 16 states, there are small nonzero “leakage” probabilities for 11 of these states in the real quantum hardware.

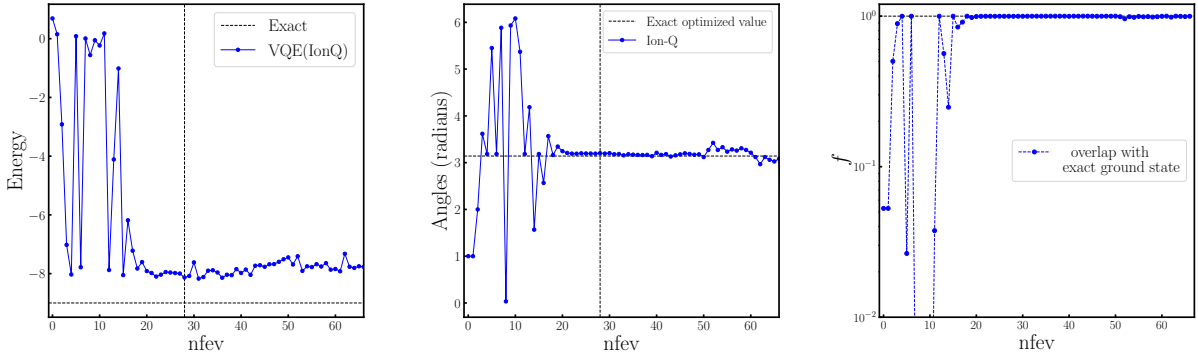


FIG. 7. Experimental results for the bubble plaquette: (left) Plot of the energy with the number of function evaluations using the quantum hardware (IonQ trapped ions). The deviation from the exact result is commented upon in the text. (middle) The estimate of the variational parameter θ at each step of the optimizer. (right) Measure of the fidelity of the variational wavefunction with the exact wavefunction at each step in the optimization process. The dashed value indicates the analytical result.

Let us consider the triangle first, where it is not possible to build the ground state by forming singlets at each site due to the frustrated nature of the lattice. Instead, the ground state is not gauge-invariant, but has two singlets at two sites, and a triplet on the third site. The corresponding energy is then $E = -(-3)^2 \cdot 1 = -9$. The wavefunction is a linear combination of three terms where the triplet can be located at the three possible sites,

$$|\psi_G\rangle = \frac{1}{\sqrt{3}} \left[|\psi_s\rangle_x |\psi_s\rangle_y |\psi_2\rangle_z + 2 \text{ permutations} \right], \quad (35)$$

where the states $|\psi_s\rangle$ and $|\psi_2\rangle$ are described in Eq. (9) and Eq. (10).

The square plaquette is made up of four links and eight spin-1/2 particles (Fig. 5). The ground state is gauge-invariant and is the product of four two-spin singlets as described in Eq. (9), with energy $E = -(-3)^4 = -81$.

We use a VQE algorithm on an exact simulator to check against analytical results for both the triangular and square plaquettes. Their variational ansätze are given

by

$$\begin{aligned}
|\psi(\theta)\rangle_{\text{tri}} &= \text{CNOT}_{01} \cdot R_z(\theta)_0 \cdot H_0 \\
&\quad \times \text{CNOT}_{23} \cdot R_z(\theta)_2 \cdot H_2 \\
&\quad \times \text{CNOT}_{45} \cdot R_z(\theta)_4 \cdot H_4 |000101\rangle, \\
|\psi(\theta)\rangle_{\text{square}} &= \\
&\quad \text{CNOT}_{01} \cdot R_z(\theta)_0 \cdot H_0 \\
&\quad \times \text{CNOT}_{23} \cdot R_z(\theta)_2 \cdot H_2 \\
&\quad \times \text{CNOT}_{45} \cdot R_z(\theta)_4 \cdot H_4 \\
&\quad \times \text{CNOT}_{67} \cdot R_z(\theta)_6 \cdot H_6 |01010101\rangle.
\end{aligned} \tag{36}$$

As in the bubble case, a single variational parameter is sufficient to parameterize the states. In Fig. 8, we present the convergence of VQE, demonstrating that the result converges to the exact analytical results. The convergence behavior is shown for two different classical optimizers, COBYLA and Powell, and in both cases COBYLA clearly outperforms the Powell method, consistent with what we observed for the bubble plaquette in Fig. 6. We compare both the ED results and the results from the VQE algorithm in Table II, using the simple VQE Ansätze defined in Eq. (36). The calculation for the VQE ansatz involves minimization of a single parameter, and could be done exactly.

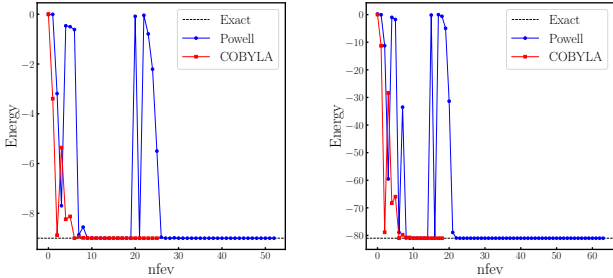


FIG. 8. Plots of the energy with the number of function evaluations for the triangular plaquette (left) and the square plaquette (right).

B. Spontaneous Symmetry Breaking with VQE, VQD and QAOA

The last section demonstrated the extraction of the ground state (GS) in the electric basis, but since the basis is not gauge-invariant, noisy hardware leads to contributions from other Gauss Law sectors. To completely eliminate any traces of gauge-variant states, here we adopt the gauge-invariant basis described in Section II. Using variational techniques in this basis, we aim at recovering not only the GS, but also the lowest-lying excitation. The ground state of the model breaks the \mathbb{Z}_2 charge conjugation symmetry spontaneously, leading to a scenario where

the GS and the first excited state are identified with \mathbb{Z}_2 -even and \mathbb{Z}_2 -odd quantum numbers respectively, and the gap between them closes exponentially with the volume.

We show that spontaneous symmetry breaking can be detected with two specific variational techniques: the first uses a generic linearly connected VQE ansatz, and the second involves QAOA-inspired ansätze for both the GS and first excited state (see Section III).

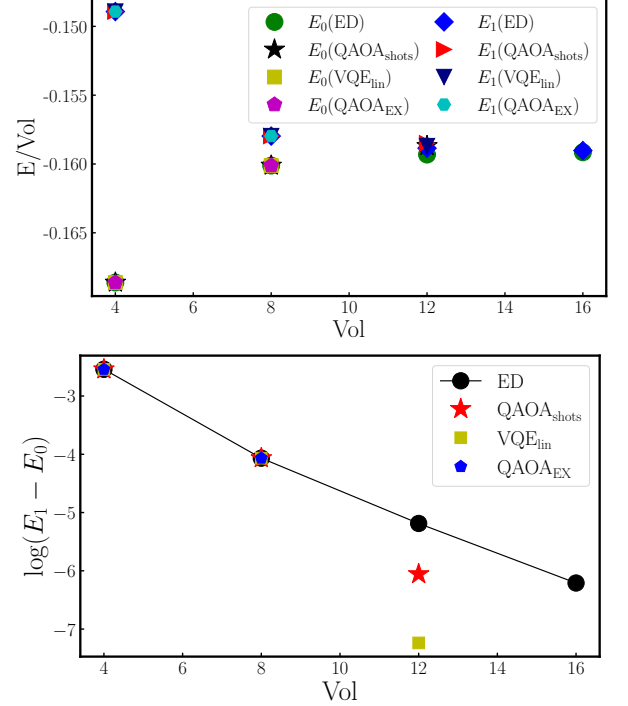


FIG. 9. (Top): Comparison of the results of ED, QAOA_{shots}, VQE_{lin}, and QAOA_{EX} by calculating E_0 and E_1 . (Bottom): The smallest energy gap ($E_1 - E_0$) for different system sizes in the pure $SO(3)$ QLM in 2-d. Note that although the extraction of the energy looks good, extraction of the gap exposes the difficulty of the problem. Both the VQE_{lin} and the QAOA_{shots} have difficulty in convergence on classical hardware with the stated circuit depth on the 2×6 lattice.

$SO(3)$ -symmetric gauge theory: For the $SO(3)$ model, we compute the two lowest-lying energies, E_0 and E_1 , at four lattice sizes: 2×2 , 2×4 , 2×6 , and 2×8 , in order to understand the behavior of the system in the thermodynamic limit. We use the gauge-invariant basis in order to study the system at these larger lattices, and we get the E_0 and E_1 using two different variational techniques. The first technique employs the linearly connected VQE ansatz defined in Eq. (21) to get the ground state, and then uses VQD with the optimized VQE state in order to get the first excited state. We use the SLSQP optimizer for these variational methods. The second technique uses the QAOA ansatz defined in Eq. (23) and Eq. (24) to get the ground state, and then for the first excited state it uses a QAOA-inspired ansatz with Eq. (23) and Eq. (26). We used the L-BFGS-B optimizer.

Lattice Geometry	N-terms in \mathcal{H}	N-qubits	Circuit Depth VQE		Ground State Energy	
			CNOT	p	ED	VQE
Bubble	9	4	1	1	-9.0	-9.0
Triangle	27	6	1	1	-9.0	-9.0
Square	81	8	1	1	-81.0	-81.0

TABLE II. Computational Resource for Bubble, Triangular, and Square plaquettes using simple VQE Ansätze.

Lattice	N-terms in \mathcal{H}	No. of Qubits	CNOT Depth		ED		VQE _{lin}		QAOA _{shots}		QAOA _{EX}	
			VQE _{lin}	QAOA	E0	E1	E0	E1	E0	E1	E0	E1
2×2	41	4	15(p=5)	665(p=5)	-0.6745	-0.5957	-0.6745	-0.5957	-0.6745	-0.5957	-0.6745	-0.5957
2×4	164	8	385(p=55)	5592(p=12)	-1.2809	-1.2638	-1.2809	-1.2638	-1.2809	-1.2637	-1.2809	-1.2638
2×6	246	12	440(p=40)	12690(p=18)	-1.9118	-1.9062	-1.9051	-1.9044	-1.9042	-1.9019	-	-
2×8	328	16	-	-	-2.5464	-2.5444	-	-	-	-	-	-

TABLE III. Computational resource and algorithms comparison for the pure $SO(3)$ QLM. In addition to QAOA calculations using a quantum circuit simulator, which we called QAOA_{shots}, we also have included a column that we used to provide checks on the QAOA where we used exact matrix multiplications to compute each parameter-dependent energy, which we called QAOA_{EX}. Since this operation scales exponentially with the volume, it is not possible to do this calculations without access to large memory nodes for the 2×6 and the 2×8 systems.

Fig. 9 summarizes the results, with the top panel showing E_0 and E_1 computed using the two variational methods as well as the ED results, and the bottom panel showing the energy gap $E_1 - E_0$ computed using these methods as a function of the volume in a semi-log plot. We use VQE_{lin} to denote simulator linearly connected variational results, QAOA_{shots} to denote simulator QAOA results, and QAOA_{EX} to denote QAOA results where each parameter-dependent energy is computed exactly rather than with simulator shots. For the VQE linearly connected ansatz and QAOA approaches, we have completed calculations on 2×2 , 2×4 , and 2×6 lattices. On the top panel of Fig. 9, we note good visual agreement between the methods with the data points on top of each other. Table III gives the numerical values: even in the most difficult case of the 2×6 lattice, the energy results agree to better than 0.1%. By plotting $\log(E_1 - E_0)$ as a function of volume, the bottom panel of Fig. 9 shows a gap that closes exponentially with the system volume. With the data from three lattice sizes, we thus have evidence of spontaneous symmetry breaking in the ground state by making use of quantum-circuit-friendly variational ansätze. Here, we note that in ED calculations, the computational time grows exponentially with the volume of the system. However, in the quantum algorithms, the computational scaling is determined by the number of layers necessary to make the ansatz sufficiently expressive to capture the ground state. While we cannot make a

statement about the scaling of the number of layers necessary to capture this gapless physics, we see from the top of Fig. 9 that the QAOA energies are close to the ED energy with linear scaling in the number of layers (for VQE we are able to achieve the same results without scaling up the layers between 2×4 and 2×6). Thus, at least for these system sizes, we are able to get a qualitative sense that the system will be gapless in the thermodynamic limit without using an ansatz with depth that scales exponentially with the volume. This would put the scaling in line with quantum Monte Carlo algorithms when there is no sign problem, such as projector quantum Monte Carlo.

For the VQE algorithm with the linearly-entangled ansatz, it is difficult to design a parameterized ansatz that respects the different symmetries of the ground state and the first excited state. In Fig. 10, we show the energy convergence as a function of circuit depth (p) for both the ground state and the first excited state energy for 2×2 and 2×4 lattices. For the 2×2 lattice, the ground state energy gets closer to the exact value as the circuit depth increases. For the first excited state, we see large fluctuations up until $p = 4$. This happens because, with smaller p , the VQD optimizer tends to mix the ground state and the first excited state, causing an overlap that may push E_1 above the exact value. As the circuit depth increases, the optimizer is able to better resolve the symmetries leading to a good convergence. We observe a similar behavior for the 2×4 lattice, where the convergence requires a much

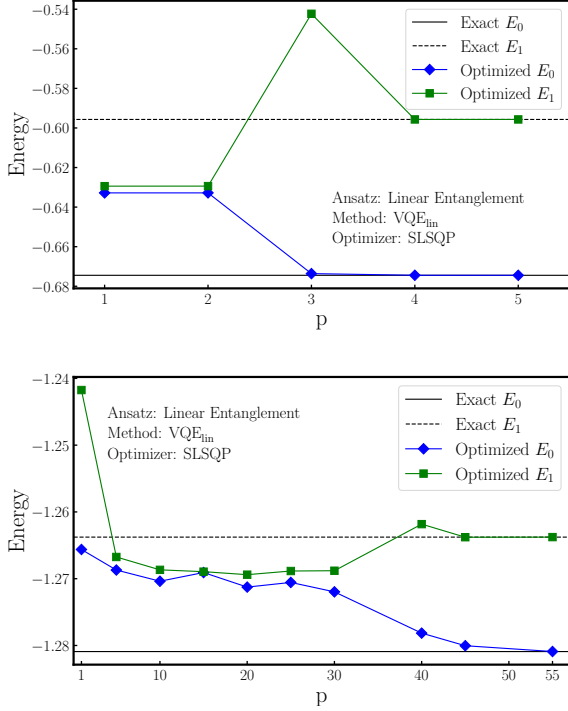


FIG. 10. (Top): Convergence of the ground state energy as a function of the circuit depth (p) on a 2×2 lattice using the VQD algorithm (VQE_{lin}). If the starting state is not created in a symmetry resolved way, the ground and the first excited states mix for lower circuit depths. However, with an increase in the circuit depth, the VQD optimizer can resolve the symmetry between these states, allowing the ground state energy to converge properly. (Bottom): The convergence of the first excited state energy for the 2×4 lattice using the VQD algorithm. The convergence occurs only at a much larger circuit depth compared to the 2×2 lattice.

At this point, we are in a good position to conjecture the method of choice as the lattice becomes wider to a two-dimensional geometry from a ladder one. The next set of lattices are 3×2 and 3×3 . The former lattice has the same symmetry breaking between the ground state and the first excited state as the ones with both even extents, and therefore, we can use the VQE algorithm on the QAOA inspired starting ansatz for the ground state and the first excited states respectively, leading to very fast convergence, as illustrated in Fig. 12 (top). However, the ground and the first excited states of the 3×3 lattice do not have any particular symmetry properties, and therefore require the VQD in conjunction with the VQE and large circuit depths. The details for the two cases are provided in the caption of Fig. 12.

larger circuit depth (p).

From Table III we also note the significantly larger circuit depth necessary for QAOA versus the linearly-entangled VQE ansatz. This is a disadvantage of the QAOA as we can see it is still possible to resolve the energy gap with the simpler linearly entangled VQE ansatz. However, an advantage that the QAOA-inspired ansätze offer over VQE/VQD is that the variational algorithm to find the first excited state is independent from the estimation of that of the ground state, which removes a potential source of error inherent to VQE/VQD for low-lying excitations.

In Fig. 11, we show the results obtained using the QAOA-inspired symmetry resolved ansätze for both the ground and the excited states. We note that while the energies themselves show agreements to better than 0.1%, the fidelities for the both the wavefunctions on the larger lattice are still several orders of magnitude larger than the smaller lattice. We point out that such considerations are important to be kept in mind while deciding the application for the quantum simulation methods. Clearly, when evaluating expectation values of local operators (such as order parameters), getting a few percent accuracy on the ground state is perhaps sufficient, while the computation of gaps in symmetry broken phase could be expensive. On the other hand, if the gaps have a $O(J)$ scaling, then the percent accuracy is enough. In summary, both methods seem to successfully capture the energies with good precision (better than 0.1%) using at most linear growth in the number of layers of the VQE/VQD ansätze as a function of system size.

V. BENCHMARK COMPUTATIONS FOR THE TRANSVERSE FIELD ISING MODEL

In order to better understand the challenge of the resolving energy gaps with variational techniques, and in particular test our QAOA-inspired ansätze in a different context, we also perform calculations for the transverse field Ising model (TFIM), which is a paradigmatic model hosting a gapped and Z_2 broken phase, separated by a second order phase transition [71]. Moreover, this calculation contrasts the complexity involved in the simulation of the fully dynamical non-Abelian $\text{SO}(3)$ lattice gauge theory in the last section. The Hamiltonian for TFIM is given by

$$H = -J \sum_{\langle i,j \rangle} \sigma_i^3 \sigma_j^3 - h_x \sum_i \sigma_i^1, \quad (37)$$

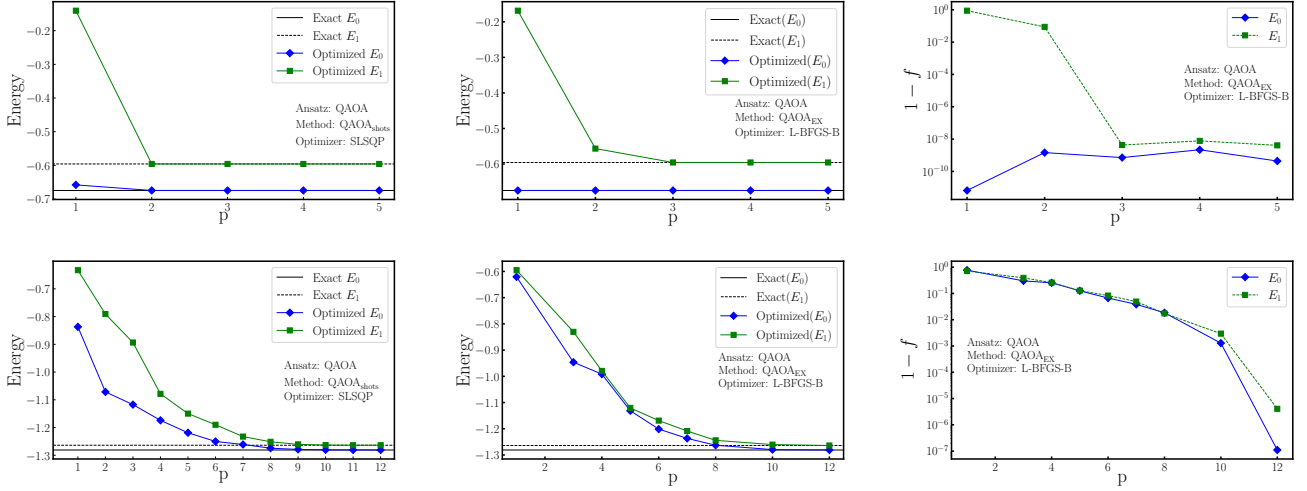


FIG. 11. Results for the energy and the fidelity as a function of circuit depth for two different lattice sizes: the top column is the result for 2×2 , while the bottom column is for 2×4 lattice. The left panel shows the ground state and the first excited state energy as a function of circuit depth (p) using the VQE algorithm ($\text{QAOA}_{\text{shots}}$); the middle panel shows the convergence of the ground state and the first excited state energy using the QAOA algorithm (QAOA_{EX}), and the right panel shows the in-fidelity with the circuit depth using the QAOA algorithm. Corresponding figures showing the convergence (restricted to our circuit depths) is shown in Fig. 15 Appendix D.

with J the interaction strength between adjacent spins, and h_x the external magnetic field. We consider $|J| = 1$ and explore three different regimes by varying the value of h_x . When $|h_x| < |J|$, the ground state breaks the spin-flip symmetry spontaneously (ferromagnetic phase). For a finite system, we expect the lowest mass gap to scale as $\exp(-\alpha V)$. When $|h_x| = 1$, the system undergoes a quantum phase transition, and for $|h_x| > |J|$, the system is in a gapped phase (paramagnetic phase).

We use the QAOA algorithm to find the smallest mass gap for different lattice sizes, dividing the Hamiltonian for our variational ansatz into

$$H_1 = -J \sum_{\langle ij \rangle} \sigma_i^3 \sigma_j^3, \quad H_2 = -h_x \sum_i \sigma_i^1. \quad (38)$$

Note that here we set H_1 to be the interaction terms rather than the magnetic field terms which we used in the $SO(3)$ example, and indeed which are typically used for QAOA for the Ising model. The QAOA ansatz is then

$$|GS\rangle_{\text{QAOA}} = \prod_{k=1}^p e^{iC_{1,k}H_1} e^{iC_{2,k}H_2} |\psi_A\rangle, \quad (39)$$

where to obtain the ground state we set $|\psi_A\rangle = 1/\sqrt{2}(|\uparrow\uparrow \dots \uparrow\rangle + |\downarrow\downarrow \dots \downarrow\rangle)$, the GHZ state. If we had built $|\psi_A\rangle$ using the transverse magnetic field terms instead (as is typically done), we would have $|\psi_A\rangle = \prod_i H_i |\uparrow\uparrow \dots \uparrow\rangle$, where $H_i (= 1/\sqrt{2}(\sigma_i^1 + \sigma_i^3))$ is the Hadamard operator acting on qubit i . The results for this other ansatz are given in the appendix in Fig. 17.

The first excited state wavefunction of H_1 is an-

tisymmetric under spin-flip symmetry. To compute the energy of the first excited state, we use the state $1/\sqrt{2}(|\uparrow\uparrow \dots \uparrow\rangle - |\downarrow\downarrow \dots \downarrow\rangle)$ as the initial ansatz state $|\psi_A\rangle$. We compare both the ED results and the results from the quantum algorithm in Table IV. We point out that for the same number of qubits (8), the CNOT circuit depth for the TFIM is 56, while it is 5592 for the $SO(3)$ model. Moreover, the desired results in the TFIM are easily obtained with circuit depths of $p \simeq 6$, while at least double the circuit depth is necessary for the $SO(3)$ model. The energy gap of the TFIM model is shown in Fig. 13, where we can see that the QAOA-inspired algorithm accurately measures the energy gap in all regimes, matching the ED results. We show the performance of QAOA in Fig. 17 in Appendix E, by plotting the ground state and first excited state energies, as well as the in-fidelity ($1-f$) with circuit depth (p) for a 1-d lattice with 10 sites. While much work has already been done to compute the ground state of the 1D TFIM using QAOA [72, 73], this extension of QAOA to compute the first excited state provides an additional proof of principle of the QAOA-inspired excited state ansatz that we have introduced in this paper.

Due to the plaquette interaction, our $SO(3)$ model has the ingredients of a 2-d model. Thus, to have a fair comparison, we have also simulated the TFIM in 2-d using our proposed methods. It becomes clear that the symmetry-resolved QAOA method does not work as well for the 2×4 lattice compared to the comparable 1-d system. Specifically, we compared the performance of the QAOA algorithm for the TFIM with periodic boundary conditions at the critical point ($h_x = 1$) on both a 1-d lattice with 8 sites and a 2-d lattice of size 2×4 . The number of

Lattice	N-terms in \mathcal{H}	N-qubits	Circuit Depth QAOA_{EX}		$h_x = 0.5$ ($E_1 - E_0$)		$h_x = 1.0$ ($E_1 - E_0$)		$h_x = 1.5$ ($E_1 - E_0$)	
			CNOT	p	ED	QAOA_{EX}	ED	QAOA_{EX}	ED	QAOA_{EX}
4	8	4	40	4	0.03549	0.03549	0.39782	0.39782	1.15446	1.15446
6	12	6	56	4	0.00689	0.00689	0.2633	0.2633	1.0523	1.0523
8	16	8	108	6	0.00146	0.00146	0.19698	0.19698	1.01945	1.01945
10	20	10	132	6	0.00032	0.0003	0.1574	0.1574	1.00757	1.00757

TABLE IV. Computational Resource and Algorithms Comparison for 1D-TFIM

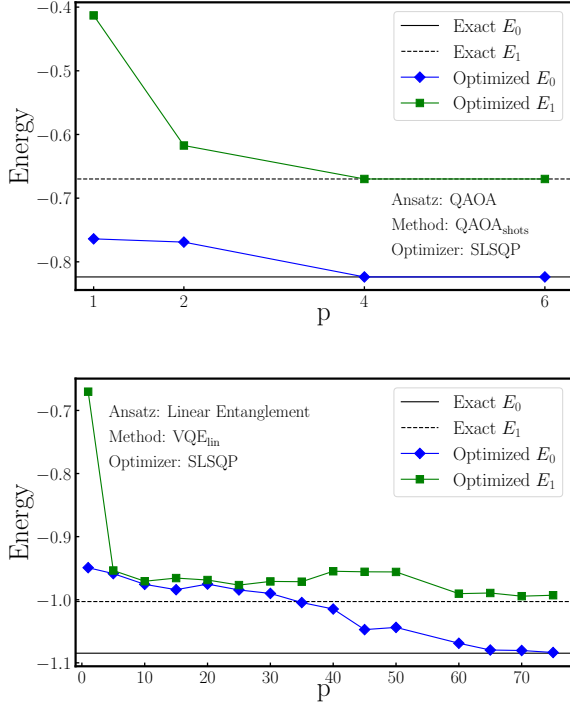


FIG. 12. (Top): Convergence plots for the ground state and the first excited state for the 3×2 lattice, which share the same symmetry breaking patterns as the other lattices. The convergence is very fast for initial states chosen in appropriate symmetry sectors. (bottom) For the 3×3 lattice, there is no symmetry breaking between the ground and first excited state, and we required a circuit depth of 600 (75 layers each of linearly entangled ansatz, with CNOT gate of depth 8) for a decent convergence. The total number of terms in the Hamiltonian is 729, and the VQE/VQD values are $E_0 = -1.08364012$ (compare with the exact value $E_0 = -1.08475104$), and $E_1 = -1.0028875$ (against the exact value $E_1 = -0.99288576$).

qubits is the same (8) in both cases. The performance is compared through the infidelity. As shown in Fig. 14, for the ground state, the 1-d lattice achieves significantly better infidelity ($1 - f$) at lower circuit depths, while the 2×4 lattice requires much larger circuit depths (p) to achieve

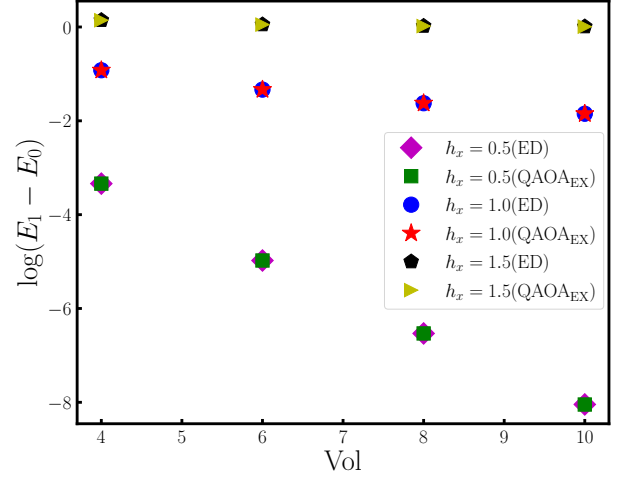


FIG. 13. Plot of the energy difference for transverse field Ising model (TFIM) in 1-d.

a comparable in-fidelity. In fact, the same behaviour was also visible for the $SO(3)$ model in the context of the 2×2 and the 2×4 lattice. Due to periodic boundary conditions, many terms cancel out in the Hamiltonian for the former lattice in contrast to the latter. The results in Fig. 11 clearly show the excellent convergence obtained for the former lattices, and the larger circuit depths required for a corresponding convergence on the 2×4 lattices.

The observed difference in convergence rate could perhaps be justified from general arguments about the entanglement structure for the ground states. Ground states of quantum systems interacting via a local Hamiltonian can exist in gapped, critical, or gapless phases. The ground states of gapped phases are expected to have an area-law for the entanglement entropy. This implies that the entanglement content of two-dimensional ground states is more than that of one dimensional counterparts, in particular if the ground state of a gapless phase is under question. The observed results indeed follow this general reasoning: to capture the ground state in two dimensions with the same precision as in one dimension, a larger circuit depth

is necessary.

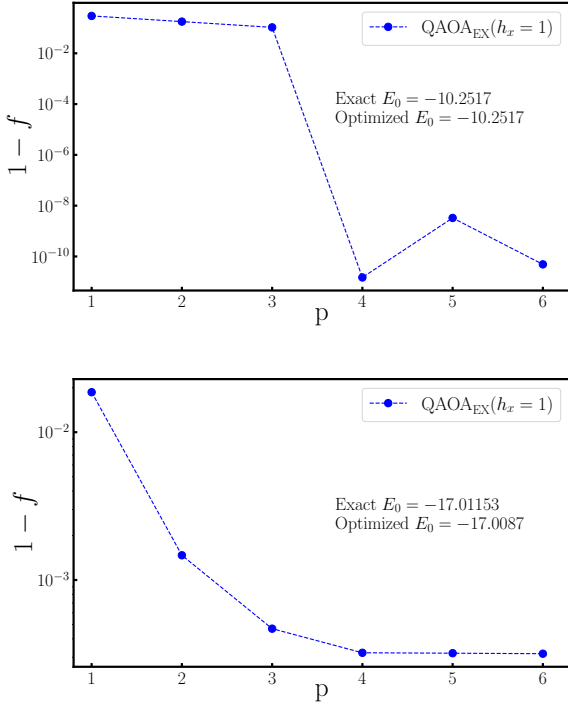


FIG. 14. (Top): Plot of the in-fidelity of the ground state of TFIM at the critical point ($h_x = 1$) with circuit depth (p) on a 1D lattice with 8 sites. (Bottom): We plot the in-fidelity of the ground state on a 2×4 lattice. The plots demonstrate that for the same circuit depth, the 1D lattice performs much better than the 2D lattice.

VI. CONCLUSION

In this article, we have explored several theoretical and experimental aspects relevant for digital quantum simulation of non-Abelian lattice gauge theories in two spatial dimensions. Until now, most quantum simulations of gauge theories have been restricted to just one spatial dimension, primarily due to the complexity of managing large-dimensional Hilbert spaces associated with gauge fields and the challenges of enforcing Gauss's law constraints.

To get around these challenges in two spatial dimension, we consider a specific quantum link model with $SO(3)$ gauge invariance in the absence of matter fields, and, explicitly demonstrate the utility of defining and working in the gauge-invariant basis. Given that this model exhibits notable nuclear physics phenomenology (such as binding, chiral symmetry breaking, and its restoration at finite density—that are also observed in nature), it is worthwhile to investigate the potential of quantum computing for studying this particular model.

While working in the electric flux basis can be intuitive

for understanding, and exact gauge-invariant results can be obtained using classical computations, implementing the problem on a quantum hardware does not always ensure that the (non-Abelian) gauge invariance is exactly maintained. We demonstrated this using the simplest possible plaquette with only two links (a bubble plaquette) on the trapped-ion IonQ quantum computers. We observe that when employing variational quantum algorithms like the VQE, the hardware generates an excess of states in the electric flux beyond what is required to accurately reproduce the gauge-invariant ground state. This is reflected in the ground state energy, which shows a deviation of approximately $\sim 10\%$ from the exact energy. However, by using a gauge-invariant ansatz for the ground state, we have reproduced the wave function with a fidelity ~ 1 .

Having justified the requirement of the gauge-invariant basis, we then formulated the variational ansätze directly in the gauge-invariant basis, and used different quantum algorithms such as the linearly connected VQE and the QAOA to explore the ground state and the first excited state of this model. The key objective was to determine the feasibility of using quantum algorithms in order to explore the scenario of SSB of a discrete symmetry, when the finite volume mass gap closes exponentially with increasing volume, which we show to be a challenging problem even in the gauge-invariant basis. Our studies explore two different strategies to combat this challenge: the first being the VQE for the ground state, and then the VQD with converged ground state to extract the excited state, and the second is the QAOA with symmetry-resolved initial states. Our results resolve energies within 0.1% using ansätze with layers that scale at most linearly with the system's volume. Further, in order to have a fair comparison of the difficulty associated with simulating SSB in non-Abelian gauge theories, we also simulate the paradigmatic TFIM which has a \mathbb{Z}_2 SSB for a range of parameters. In both the models, we demonstrate the necessity of using a symmetry-resolved variational ansatz in order to capture the ground state and first excited state with different symmetries.

Another significant issue highlighted in our paper is the impact of higher than one spatial dimensionality. While various variational quantum algorithms have demonstrated remarkable success for quantum systems in one spatial dimension, their performance degrades notably when applied to genuinely two-dimensional systems. Although energy estimates remain accurate within a few percent, the fidelities of the resulting ground state wavefunctions are orders of magnitude lower. This phenomenon persists even for well-studied models like the paradigmatic TFIM. Therefore, the development of more effective quantum algorithms for systems in higher spatial dimensions remains an open and pressing challenge.

Our results pave the way for various new investigations: the most immediate is to include fermions in the problem, and explore how the quantum algorithms fare in the presence of fermions. This presents a significant

challenge, as it requires the development of efficient fermion-to-qubit encoding schemes that maintain a high degree of locality, particularly in two-dimensional systems. The phenomenology of the $SO(3)$ model with fermions is expected to be richer in two spatial dimensions as compared to the previously studied one dimensional model because the magnetic field term can play a non-trivial role and generate more phases. We are currently investigating these aspects in detail. In terms of quantum computing, the circuits developed here with considerable theoretical insights need to be implemented on actual quantum hardware for the larger systems in order to understand their scaling. It is possible to place external charges in the pure gauge theory, and study the string breaking for a non-Abelian gauge theory on a quantum hardware.

Acknowledgments: We would like to thank Aditya

Banerjee, Shailesh Chandrasekharan, Arti Garg, Graham van Goffrier, Arnab Kundu, Marina Marinkovic, Nilmani Mathur, Indrakshi Roychowdhury, Arnab Sen, and Uwe-Jens Wiese for various illuminating conversations. Research of BC at the University of Southampton has been supported by the following research fellowship and grants - Leverhulme Trust (ECF-2019-223 G100820), STFC (Grant no. ST/X000583/1), STFC (Grant no. ST/W006251/1), and EPSRC (Grant no. EP/W032635/1). Research of EH at Perimeter Institute is supported in part by the Government of Canada through the Department of Innovation, Science and Industry Canada and by the Province of Ontario through the Ministry of Colleges and Universities. We acknowledge access to Ion Q through the AWS Cloud Credit for Research program and thank Sebastian Hassinger and Sebastian Stern for help with experiments.

-
- [1] F. J. Dyson, “The radiation theories of tomonaga, schwinger, and feynman,” *Phys. Rev.* **75**, 486–502 (1949).
 - [2] Kenneth G. Wilson, “Confinement of quarks,” *Phys. Rev. D* **10**, 2445–2459 (1974).
 - [3] P. Weisz and P. Majumdar, “Lattice gauge theories,” *Scholarpedia* **7**, 8615 (2012), revision #137037.
 - [4] Michael Creutz, “LATTICE GAUGE THEORIES AND MONTE CARLO ALGORITHMS,” in *XIX International Seminar on Theoretical Physics: Nonperturbative Aspects of the Standard Model (GIFT Seminar)* (1988).
 - [5] I. Montvay, “Monte Carlo Methods in Quantum Field Theory,” in *Taller de Altas Energias: Spring School on High Energy Physics* (2007) [arXiv:0705.4356 \[hep-lat\]](#).
 - [6] Yannick Meurice, James C. Osborn, Ryo Sakai, Judah Unmuth-Yockey, Simon Catterall, and Rolando D. Somma, “Tensor networks for high energy physics: contribution to snowmass 2021,” (2022), [arXiv:2203.04902 \[hep-lat\]](#).
 - [7] Mari Carmen Bañuls, “Tensor network algorithms: A route map,” *Annual Review of Condensed Matter Physics* **14**, 173–191 (2023).
 - [8] Giovanni Cataldi, Giuseppe Magnifico, Pietro Silvi, and Simone Montangero, “Simulating $(2+1)$ D $su(2)$ yang-mills lattice gauge theory at finite density with tensor networks,” *Phys. Rev. Res.* **6**, 033057 (2024).
 - [9] Paul Benioff, “The computer as a physical system: A microscopic quantum mechanical Hamiltonian model of computers as represented by Turing machines,” *Journal of Statistical Physics* **22**, 563–591 (1980).
 - [10] Richard P. Feynman, “Simulating Physics with Computers,” *International Journal of Theoretical Physics* **21**, 467–488 (1982).
 - [11] Dimitris G. Angelakis and Changsuk Noh, “Quantum simulations and many-body physics with light,” *Rept. Prog. Phys.* **80**, 016401 (2016).
 - [12] Morten Kjaergaard, Mollie E. Schwartz, Jochen Braumüller, Philip Krantz, Joel I-Jan Wang, Simon Gustavsson, and William D. Oliver, “Superconducting Qubits: Current State of Play,” *Physics* **11**, 369–395 (2020), [arXiv:1905.13641 \[quant-ph\]](#).
 - [13] Lawrence W. Cheuk, Matthew A. Nichols, Melih Okan, Thomas Gersdorf, Vinay V. Ramasesh, Waseem S. Bakr, Thomas Lompe, and Martin W. Zwierlein, “Quantum-Gas Microscope for Fermionic Atoms,” *Phys. Rev. Lett.* **114**, 193001 (2015).
 - [14] Z. Hadzibabic, C. A. Stan, K. Dieckmann, S. Gupta, M. W. Zwierlein, A. Görlitz, and W. Ketterle, “Two-species mixture of quantum degenerate bose and fermi gases,” *Phys. Rev. Lett.* **88**, 160401 (2002).
 - [15] Ehud Altman *et al.*, “Quantum Simulators: Architectures and Opportunities,” *PRX Quantum* **2**, 017003 (2021), [arXiv:1912.06938 \[quant-ph\]](#).
 - [16] C. Monroe *et al.*, “Programmable quantum simulations of spin systems with trapped ions,” *Rev. Mod. Phys.* **93**, 025001 (2021), [arXiv:1912.07845 \[quant-ph\]](#).
 - [17] Giulia Semeghini *et al.*, “Probing topological spin liquids on a programmable quantum simulator,” *Science* **374**, abi8794 (2021), [arXiv:2104.04119 \[quant-ph\]](#).
 - [18] D. Bluvstein *et al.*, “Controlling quantum many-body dynamics in driven Rydberg atom arrays,” *Science* **371**, 1355–1359 (2021).
 - [19] Michael Foss-Feig, Guido Pagano, Andrew C. Potter, and Norman Y. Yao, “Progress in trapped-ion quantum simulation,” (2024), [arXiv:2409.02990 \[quant-ph\]](#).
 - [20] Jarrod R. McClean, Jonathan Romero, Ryan Babbush, and Alán Aspuru-Guzik, “The theory of variational hybrid quantum-classical algorithms,” *New J. Phys.* **18**, 023023 (2016), [arXiv:1509.04279 \[quant-ph\]](#).
 - [21] J. Zhang, G. Pagano, P. W. Hess, A. Kyprianidis, P. Becker, H. Kaplan, A. V. Gorshkov, Z. X. Gong, and C. Monroe, “Observation of a many-body dynamical phase transition with a 53-qubit quantum simulator,” *Nature* **551**, 601–604 (2017), [arXiv:1708.01044 \[quant-ph\]](#).
 - [22] Abhinav Kandala, Kristan Temme, Antonio D. Corcoles, Antonio Mezzacapo, Jerry M. Chow, and Jay M. Gambetta, “Error mitigation extends the computational reach of a noisy quantum processor,” *Nature* **567**, 491–495 (2019), [arXiv:1805.04492 \[quant-ph\]](#).
 - [23] Christian W. Bauer, Wibe A. de Jong, Benjamin Nachman, and Davide Provasoli, “Quantum Algorithm for

- High Energy Physics Simulations,” *Phys. Rev. Lett.* **126**, 062001 (2021), [arXiv:1904.03196 \[hep-ph\]](#).
- [24] Anthony Ciavarella, “Algorithm for quantum computation of particle decays,” *Phys. Rev. D* **102**, 094505 (2020), [arXiv:2007.04447 \[hep-th\]](#).
- [25] Benjamin Hall, Alessandro Roggero, Alessandro Baroni, and Joseph Carlson, “Simulation of collective neutrino oscillations on a quantum computer,” *Phys. Rev. D* **104**, 063009 (2021), [arXiv:2102.12556 \[quant-ph\]](#).
- [26] Adrián Pérez-Salinas, Juan Cruz-Martinez, Abdulla A. Alhajri, and Stefano Carrazza, “Determining the proton content with a quantum computer,” *Phys. Rev. D* **103**, 034027 (2021), [arXiv:2011.13934 \[hep-ph\]](#).
- [27] Emilie Huffman, Miguel García Vera, and Debasish Banerjee, “Toward the real-time evolution of gauge-invariant \mathbb{Z}_2 and $U(1)$ quantum link models on noisy intermediate-scale quantum hardware with error mitigation,” *Phys. Rev. D* **106**, 094502 (2022), [arXiv:2109.15065 \[quant-ph\]](#).
- [28] Angus Kan, Lena Funcke, Stefan Kühn, Luca Dellantonio, Jinglei Zhang, Jan F. Haase, Christine A. Muschik, and Karl Jansen, “Investigating a (3+1)D topological θ -term in the Hamiltonian formulation of lattice gauge theories for quantum and classical simulations,” *Phys. Rev. D* **104**, 034504 (2021), [arXiv:2105.06019 \[hep-lat\]](#).
- [29] Thomas D. Cohen, Henry Lamm, Scott Lawrence, and Yukari Yamauchi (NuQS), “Quantum algorithms for transport coefficients in gauge theories,” *Phys. Rev. D* **104**, 094514 (2021), [arXiv:2104.02024 \[hep-lat\]](#).
- [30] Lukas Homeier, Annabelle Bohrdt, Simon Linsel, Eugene Demler, Jad C. Halimeh, and Fabian Grusdt, “Realistic scheme for quantum simulation of \mathbb{Z}_2 lattice gauge theories with dynamical matter in (2+1)D,” *Commun. Phys.* **6**, 127 (2023), [arXiv:2205.08541 \[cond-mat.quant-gas\]](#).
- [31] Pierpaolo Fontana, Joao C. Pinto Barros, and Andrea Trombettoni, “Quantum simulator of link models using spinor dipolar ultracold atoms,” *Phys. Rev. A* **107**, 043312 (2023), [arXiv:2210.14836 \[cond-mat.quant-gas\]](#).
- [32] Jesse Osborne, Ian P. McCulloch, Bing Yang, Philipp Hauke, and Jad C. Halimeh, “Large-Scale 2 + 1D $U(1)$ Gauge Theory with Dynamical Matter in a Cold-Atom Quantum Simulator,” (2022), [arXiv:2211.01380 \[cond-mat.quant-gas\]](#).
- [33] Christian W. Bauer *et al.*, “Quantum Simulation for High-Energy Physics,” *PRX Quantum* **4**, 027001 (2023), [arXiv:2204.03381 \[quant-ph\]](#).
- [34] Roland C. Farrell, Marc Illa, Anthony N. Ciavarella, and Martin J. Savage, “Quantum simulations of hadron dynamics in the Schwinger model using 112 qubits,” *Phys. Rev. D* **109**, 114510 (2024), [arXiv:2401.08044 \[quant-ph\]](#).
- [35] Uwe-Jens Wiese, “Ultracold Quantum Gases and Lattice Systems: Quantum Simulation of Lattice Gauge Theories,” *Annalen Phys.* **525**, 777–796 (2013), [arXiv:1305.1602 \[quant-ph\]](#).
- [36] Erez Zohar, Alessandro Farace, Benni Reznik, and J. Ignacio Cirac, “Digital lattice gauge theories,” *Phys. Rev. A* **95**, 023604 (2017), [arXiv:1607.08121 \[quant-ph\]](#).
- [37] Sergey B. Bravyi and Alexei Yu. Kitaev, “Fermionic Quantum Computation,” *Annals Phys.* **298**, 210–226 (2002), [arXiv:quant-ph/0003137](#).
- [38] Danny Paulson *et al.*, “Simulating 2D Effects in Lattice Gauge Theories on a Quantum Computer,” *PRX Quantum* **2**, 030334 (2021), [arXiv:2008.09252 \[quant-ph\]](#).
- [39] Zohreh Davoudi, Indrakshi Raychowdhury, and Andrew Shaw, “Search for efficient formulations for Hamiltonian simulation of non-Abelian lattice gauge theories,” *Phys. Rev. D* **104**, 074505 (2021), [arXiv:2009.11802 \[hep-lat\]](#).
- [40] Tanmoy Bhattacharya, Alexander J. Buser, Shailesh Chandrasekharan, Rajan Gupta, and Hersh Singh, “Qubit regularization of asymptotic freedom,” *Phys. Rev. Lett.* **126**, 172001 (2021), [arXiv:2012.02153 \[hep-lat\]](#).
- [41] Andrei Alexandru, Paulo F. Bedaque, Siddhartha Harmalkar, Henry Lamm, Scott Lawrence, and Neill C. Warrington (NuQS), “Gluon Field Digitization for Quantum Computers,” *Phys. Rev. D* **100**, 114501 (2019), [arXiv:1906.11213 \[hep-lat\]](#).
- [42] Anthony Ciavarella, Natalie Klco, and Martin J. Savage, “Trailhead for quantum simulation of $SU(3)$ Yang-Mills lattice gauge theory in the local multiplet basis,” *Phys. Rev. D* **103**, 094501 (2021), [arXiv:2101.10227 \[quant-ph\]](#).
- [43] Yannick Meurice, “Theoretical methods to design and test quantum simulators for the compact Abelian Higgs model,” *Phys. Rev. D* **104**, 094513 (2021), [arXiv:2107.11366 \[quant-ph\]](#).
- [44] Torsten V. Zache, Maarten Van Damme, Jad C. Halimeh, Philipp Hauke, and Debasish Banerjee, “Toward the continuum limit of a (1+1)D quantum link Schwinger model,” *Phys. Rev. D* **106**, L091502 (2022), [arXiv:2104.00025 \[hep-lat\]](#).
- [45] Hanqing Liu and Shailesh Chandrasekharan, “Qubit Regularization and Qubit Embedding Algebras,” *Symmetry* **14**, 305 (2022), [arXiv:2112.02090 \[hep-lat\]](#).
- [46] Erik Gustafson, “Prospects for Simulating a Qudit Based Model of (1+1)d Scalar QED,” *Phys. Rev. D* **103**, 114505 (2021), [arXiv:2104.10136 \[quant-ph\]](#).
- [47] Saurabh V. Kadam, Indrakshi Raychowdhury, and Jesse R. Stryker, “Loop-string-hadron formulation of an $SU(3)$ gauge theory with dynamical quarks,” *Phys. Rev. D* **107**, 094513 (2023), [arXiv:2212.04490 \[hep-lat\]](#).
- [48] Debasish Banerjee, Emilie Huffman, and Lukas Rammelmüller, “Exploring bosonic and fermionic link models on (3+1)D tubes,” *Phys. Rev. Res.* **4**, 033174 (2022), [arXiv:2201.07171 \[hep-lat\]](#).
- [49] Andrei Alexandru, Paulo F. Bedaque, Andrea Carosso, Michael J. Cervia, Edison M. Muraire, and Andy Sheng, “Fuzzy gauge theory for quantum computers,” *Phys. Rev. D* **109**, 094502 (2024), [arXiv:2308.05253 \[hep-lat\]](#).
- [50] Saurabh V. Kadam, Aahiri Naskar, Indrakshi Raychowdhury, and Jesse R. Stryker, “Loop-string-hadron approach to $SU(3)$ lattice Yang-Mills theory: Gauge invariant Hilbert space of a trivalent vertex,” (2024), [arXiv:2407.19181 \[hep-lat\]](#).
- [51] Pierpaolo Fontana, Marc Miranda Riaza, and Alessio Celi, “An efficient finite-resource formulation of non-abelian lattice gauge theories beyond one dimension,” (2024), [arXiv:2409.04441 \[quant-ph\]](#).
- [52] John Preskill, “Quantum Computing in the NISQ era and beyond,” *Quantum* **2**, 79 (2018), [arXiv:1801.00862 \[quant-ph\]](#).
- [53] Jules Tilly *et al.*, “The Variational Quantum Eigensolver: A review of methods and best practices,” *Phys. Rept.* **986**, 1–128 (2022), [arXiv:2111.05176 \[quant-ph\]](#).
- [54] Abhinav Kandala, Antonio Mezzacapo, Kristan Temme, Maika Takita, Markus Brink, Jerry M. Chow, and Jay M. Gambetta, “Hardware-efficient variational quantum eigensolver for small molecules and quantum magnets,” *Nature* **549**, 242–246 (2017).
- [55] Sukin Sim, Peter D. Johnson, and Alán Aspuru-Guzik, “Expressibility and Entangling Capability of Parameter-

- ized Quantum Circuits for Hybrid Quantum-Classical Algorithms,” *Adv. Quantum Technol.* **2**, 1900070 (2019), [arXiv:1905.10876 \[quant-ph\]](#).
- [56] Oscar Higgott, Daochen Wang, and Stephen Brierley, “Variational Quantum Computation of Excited States,” *Quantum* **3**, 156 (2019), [arXiv:1805.08138 \[quant-ph\]](#).
- [57] Edward Farhi, Jeffrey Goldstone, and Sam Gutmann, “A Quantum Approximate Optimization Algorithm,” (2014), [arXiv:1411.4028 \[quant-ph\]](#).
- [58] Leo Zhou, Sheng-Tao Wang, Soonwon Choi, Hannes Pichler, and Mikhail D. Lukin, “Quantum Approximate Optimization Algorithm: Performance, Mechanism, and Implementation on Near-Term Devices,” *Phys. Rev. X* **10**, 021067 (2020), [arXiv:1812.01041 \[quant-ph\]](#).
- [59] Gavin E. Crooks, “Performance of the Quantum Approximate Optimization Algorithm on the Maximum Cut Problem,” (2018), [arXiv:1811.08419 \[quant-ph\]](#).
- [60] Martin Larocca, Piotr Czarnik, Kunal Sharma, Gopikrishnan Muraleedharan, Patrick J. Coles, and M. Cerezo, “Diagnosing Barren Plateaus with Tools from Quantum Optimal Control,” *Quantum* **6**, 824 (2022), [arXiv:2105.14377 \[quant-ph\]](#).
- [61] P.C. Hohenberg and A.P. Krekhov, “An introduction to the ginzburg-landau theory of phase transitions and nonequilibrium patterns,” *Physics Reports* **572**, 1–42 (2015), an introduction to the Ginzburg–Landau theory of phase transitions and nonequilibrium patterns.
- [62] S. Chandrasekharan and U. J. Wiese, “Quantum link models: A Discrete approach to gauge theories,” *Nucl. Phys. B* **492**, 455–474 (1997), [arXiv:hep-lat/9609042](#).
- [63] E. Rico, M. Dalmonte, P. Zoller, D. Banerjee, M. Bögli, P. Stebler, and U. J. Wiese, “SO(3) ”Nuclear Physics” with ultracold Gases,” *Annals Phys.* **393**, 466–483 (2018), [arXiv:1802.00022 \[cond-mat.quant-gas\]](#).
- [64] R. Brower, S. Chandrasekharan, and U.-J. Wiese, “Qcd as a quantum link model,” *Physical Review D* **60** (1999), [10.1103/physrevd.60.094502](#).
- [65] D. Banerjee, M. Bögli, M. Dalmonte, E. Rico, P. Stebler, U. J. Wiese, and P. Zoller, “Atomic Quantum Simulation of U(N) and SU(N) Non-Abelian Lattice Gauge Theories,” *Phys. Rev. Lett.* **110**, 125303 (2013), [arXiv:1211.2242 \[cond-mat.quant-gas\]](#).
- [66] D. Banerjee, F. J. Jiang, P. Widmer, and U. J. Wiese, “The $(2 + 1)$ -d U(1) quantum link model masquerading as deconfined criticality,” *J. Stat. Mech.* **1312**, P12010 (2013), [arXiv:1303.6858 \[cond-mat.str-el\]](#).
- [67] A. Banerjee, D. Banerjee, G. Kanwar, A. Mariani, T. Rindlisbacher, and U. J. Wiese, “Broken symmetry and fractionalized flux strings in a staggered U(1) pure gauge theory,” *Phys. Rev. D* **109**, 014506 (2024), [arXiv:2309.17109 \[hep-lat\]](#).
- [68] Seth Lloyd, “Quantum approximate optimization is computationally universal,” (2018), [arXiv:1812.11075 \[quant-ph\]](#).
- [69] Mauro ES Morales, Jacob D Biamonte, and Zoltán Zimborás, “On the universality of the quantum approximate optimization algorithm,” *Quantum Information Processing* **19**, 1–26 (2020).
- [70] Edward Farhi, Jeffrey Goldstone, Sam Gutmann, and Michael Sipser, “Quantum Computation by Adiabatic Evolution,” (2000), [arXiv:quant-ph/0001106](#).
- [71] R. J. Elliott, P. Pfeuty, and C. Wood, “Ising model with a transverse field,” *Phys. Rev. Lett.* **25**, 443–446 (1970).
- [72] Zheng-Hang Sun, Yong-Yi Wang, Jian Cui, and Heng Fan, “Improving the performance of quantum approximate optimization for preparing non-trivial quantum states without translational symmetry,” *New J. Phys.* **25**, 013015 (2023), [arXiv:2206.02637 \[quant-ph\]](#).
- [73] Yu-Qin Chen, Shi-Xin Zhang, Chang-Yu Hsieh, and Shengyu Zhang, “Non-hermitian ground-state-searching algorithm enhanced by a variational toolbox,” *Phys. Rev. A* **107**, 042418 (2023).

Appendix A: Gauge transformation of the quantum link operators

The commutation relations for $L_{x,y}^a$, $R_{x,y}^a$ and $O_{x,y}^{ab}$ are

$$\begin{aligned} [L_{x,y}^a, O_{x,y}^{bc}] &= -t_{bd}^a O_{x,y}^{dc} \\ [R_{x,y}^a, O_{x,y}^{bc}] &= O_{x,y}^{bd} t_{dc}^a \end{aligned} \quad (\text{A1})$$

The link operator $O_{x,y}^{ab}$ transforms under gauge transformation as

$$\begin{aligned} O_{x,y}^{ab} &\longrightarrow \exp(-i(\alpha_x^m L_{x,y}^m + \alpha_y^m R_{x,y}^m)) O_{x,y}^{ab} \\ &\quad \exp(i(\alpha_x^m L_{x,y}^m + \alpha_y^m R_{x,y}^m)) \\ &= (1 - i\alpha_x^m L_{x,y}^m - i\alpha_y^m R_{x,y}^m - \mathcal{O}(\alpha^2)) O_{x,y}^{ab} \\ &\quad (1 + i\alpha_x^m L_{x,y}^m + i\alpha_y^m R_{x,y}^m + \mathcal{O}(\alpha^2)) \\ &= O_{x,y}^{ab} + i\alpha_x^m O_{x,y}^{ab} L_{x,y}^m + i\alpha_y^m O_{x,y}^{ab} R_{x,y}^m \\ &\quad - i\alpha_x^m L_{x,y}^m O_{x,y}^{ab} - i\alpha_y^m R_{x,y}^m O_{x,y}^{ab} + \mathcal{O}(\alpha^2) \\ &= O_{x,y}^{ab} - i\alpha_x^m [L_{x,y}^m, O_{x,y}^{ab}] - i\alpha_y^m [R_{x,y}^m, O_{x,y}^{ab}] + \mathcal{O}(\alpha^2) \\ &= O_{x,y}^{ab} + i\alpha_x^m t_{ac}^m O_{x,y}^{cb} - i\alpha_y^m O_{x,y}^{ac} t_{cb}^m + \mathcal{O}(\alpha^2) \\ &= (1 + i\alpha_x^m t_{ac}^m + \mathcal{O}(\alpha^2)) O_{x,y}^{cd} (1 - i\alpha_y^m t_{db}^m - \mathcal{O}(\alpha^2)) \\ &= [\exp(i\alpha_x^m t_{ac}^m)]^{ac} O_{x,y}^{cd} [\exp(-i\alpha_y^m t_{db}^m)]^{db} \end{aligned} \quad (\text{A2})$$

Appendix B: Expression of the Hamiltonian in the gauge-invariant basis

In this section, we show the relevant algebra to deduce the form of the Hamiltonian in the gauge invariant basis. We refer the reader to Fig. 2 top right, which shows four spins, labelled as $\sigma_{x,+\nu}^b$, $\sigma_{x,+\mu}^a$, $\sigma_{x,-\nu}^b$, and $\sigma_{x,-\mu}^a$ on the four links starting from the twelve o'clock position as we move in a clockwise fashion. The two gauge invariant states which can be defined on the site x are

$$\begin{aligned} |\psi_{1s}\rangle &= \frac{1}{2} [|\uparrow\uparrow\downarrow\downarrow\rangle - |\uparrow\downarrow\uparrow\downarrow\rangle - |\downarrow\uparrow\uparrow\downarrow\rangle + |\downarrow\downarrow\uparrow\uparrow\rangle], \\ |\psi_{2s}\rangle &= \frac{1}{2\sqrt{3}} [-2|\uparrow\uparrow\downarrow\downarrow\rangle - 2|\downarrow\downarrow\uparrow\uparrow\rangle \\ &\quad + |\uparrow\downarrow\uparrow\downarrow\rangle + |\downarrow\uparrow\uparrow\downarrow\rangle + |\uparrow\downarrow\downarrow\uparrow\rangle + |\downarrow\uparrow\downarrow\uparrow\rangle] \end{aligned} \quad (\text{B1})$$

Next, note that there are four plaquettes which will touch the Gauss Law vertex in the four corners, and each corner will use a different pair of spins. The plaquette touching the top right uses the pair $\vec{\sigma}_{x,+\nu}/2 \cdot \vec{\sigma}_{x,+\mu}/2$, while the plaquette touching the bottom left will use the pair $\vec{\sigma}_{x,-\mu}/2 \cdot \vec{\sigma}_{x,-\nu}/2$. The factors of 2 come from the identification $S = \sigma/2$. To obtain the matrix representation of these operators in the gauge invariant basis space, we need to evaluate the operators using the generic expansion $\vec{S}_1 \cdot \vec{S}_2 = \frac{1}{2}(S_1^+ \cdot S_2^- + S_1^- \cdot S_2^+) + S_1^z \cdot S_2^z$ in the Hilbert space spanned by $|\psi_{1s}\rangle$ and $|\psi_{2s}\rangle$. For our four

operators, we obtain:

$$\frac{\vec{\sigma}_{x,+\nu}}{2} \cdot \frac{\vec{\sigma}_{x,+\mu}}{2} = \begin{pmatrix} 0 & \frac{\sqrt{3}}{4} \\ \frac{\sqrt{3}}{4} & -\frac{1}{2} \end{pmatrix} = \frac{1}{4}(\sqrt{3}\tau^1 - I + \tau^3), \quad (\text{B2})$$

$$\frac{\vec{\sigma}_{x,-\mu}}{2} \cdot \frac{\vec{\sigma}_{x,+\nu}}{2} = \begin{pmatrix} 0 & -\frac{\sqrt{3}}{4} \\ -\frac{\sqrt{3}}{4} & -\frac{1}{2} \end{pmatrix} \quad (\text{B3})$$

$$= \frac{1}{4}(-\sqrt{3}\tau^1 - I + \tau^3), \quad (\text{B4})$$

$$\frac{\vec{\sigma}_{x,+\nu}}{2} \cdot \frac{\vec{\sigma}_{x,+\mu}}{2} = \frac{\vec{\sigma}_{x,-\mu}}{2} \cdot \frac{\vec{\sigma}_{x,-\nu}}{2}, \quad (\text{B5})$$

$$\frac{\vec{\sigma}_{x,-\mu}}{2} \cdot \frac{\vec{\sigma}_{x,+\nu}}{2} = \frac{\vec{\sigma}_{x,+\mu}}{2} \cdot \frac{\vec{\sigma}_{x,-\nu}}{2}. \quad (\text{B6})$$

Here τ^i operates in the 2×2 gauge invariant space and I is the 2×2 identity matrix. The plaquette term (by symmetry) then picks up these two types of corner operators, and has the form as given in Eq. (16) in the main text.

Appendix C: Hamiltonian decomposition for 2×4 lattice

The Hamiltonian for the 2×4 lattice was decomposed into twenty-four pieces for implementation with QAOA (each of these terms operate in the gauge-invariant subspace represented by the τ^i operators):

$$\begin{aligned} H_1 &= \frac{1}{2 \cdot 4^3} \sum_{x=1}^8 \tau_x^3, \\ H_2 &= -\frac{1}{2 \cdot 4^3} \sum_{x \neq y} \tau_x^3 \tau_y^3 + \frac{1}{2 \cdot 4^3} \sum_{x \neq y \neq z} \tau_x^3 \tau_y^3 \tau_z^3 \\ &\quad - \frac{1}{2 \cdot 4^3} (\tau_1^3 \tau_2^3 (\tau_3^3 \tau_4^3 + \tau_7^3 \tau_8^3) + \tau_5^3 \tau_6^3 (\tau_3^3 \tau_4^3 + \tau_7^3 \tau_8^3)), \\ H_3 &= -\frac{3}{2 \cdot 4^3} \tau_3^1 \tau_4^1 (-\tau_1^3 \tau_2^3 - \tau_5^3 \tau_6^3 + \tau_1^3 + \tau_2^3 + \tau_5^3 + \tau_6^3 - 2I), \\ H_4 &= -\frac{3}{2 \cdot 4^3} \tau_2^1 \tau_4^1 (-\tau_1^3 \tau_3^3 + \tau_1^3 + \tau_3^3 - I), \\ H_5 &= -\frac{3}{2 \cdot 4^3} \tau_1^1 \tau_4^1 (\tau_2^3 \tau_3^3 - \tau_2^3 - \tau_3^3 + I), \\ H_6 &= -\frac{3}{2 \cdot 4^3} \tau_2^1 \tau_3^1 (\tau_1^3 \tau_4^3 - \tau_1^3 - \tau_4^3 + I), \\ H_7 &= -\frac{3}{2 \cdot 4^3} \tau_1^1 \tau_3^1 (-\tau_2^3 \tau_4^3 + \tau_2^3 + \tau_4^3 - I), \\ H_8 &= -\frac{3}{2 \cdot 4^3} \tau_1^1 \tau_2^1 (-\tau_3^3 \tau_4^3 - \tau_7^3 \tau_8^3 + \tau_3^3 + \tau_4^3 + \tau_7^3 + \tau_8^3 - 2I), \\ H_9 &= -\frac{3}{2 \cdot 4^3} \tau_5^1 \tau_6^1 (-\tau_3^3 \tau_4^3 - \tau_7^3 \tau_8^3 + \tau_3^3 + \tau_4^3 + \tau_7^3 + \tau_8^3 - 2I), \\ H_{10} &= -\frac{3}{2 \cdot 4^3} \tau_4^1 \tau_6^1 (-\tau_3^3 \tau_5^3 + \tau_3^3 + \tau_5^3 - I), \\ H_{11} &= -\frac{3}{2 \cdot 4^3} \tau_3^1 \tau_6^1 (\tau_4^3 \tau_5^3 - \tau_4^3 - \tau_5^3 + I), \end{aligned}$$

$$\begin{aligned}
H_{12} &= -\frac{3}{2 \cdot 4^3} \tau_3^1 \tau_5^1 (-\tau_4^3 \tau_6^3 + \tau_4^3 + \tau_6^3 - I), \\
H_{13} &= -\frac{3}{2 \cdot 4^3} \tau_4^1 \tau_5^1 (\tau_3^3 \tau_6^3 - \tau_3^3 - \tau_6^3 + I), \\
H_{14} &= -\frac{3}{2 \cdot 4^3} \tau_5^1 \tau_7^1 (-\tau_6^3 \tau_8^3 + \tau_6^3 + \tau_8^3 - I), \\
H_{15} &= -\frac{3}{2 \cdot 4^3} \tau_6^1 \tau_7^1 (\tau_5^3 \tau_8^3 - \tau_5^3 - \tau_8^3 + I), \\
H_{16} &= -\frac{3}{2 \cdot 4^3} \tau_5^1 \tau_8^1 (\tau_6^3 \tau_7^3 - \tau_6^3 - \tau_7^3 + I), \\
H_{17} &= -\frac{3}{2 \cdot 4^3} \tau_7^1 \tau_8^1 (-\tau_5^3 \tau_6^3 - \tau_1^3 \tau_2^3 + \tau_1^3 + \tau_2^3 + \tau_5^3 + \tau_6^3 - 2I), \\
H_{18} &= -\frac{3}{2 \cdot 4^3} \tau_2^1 \tau_8^1 (-\tau_1^3 \tau_7^3 + \tau_1^3 + \tau_7^3 - I), \\
H_{19} &= -\frac{3}{2 \cdot 4^3} \tau_1^1 \tau_8^1 (\tau_2^3 \tau_7^3 - \tau_2^3 - \tau_7^3 + I), \\
H_{20} &= -\frac{3}{2 \cdot 4^3} \tau_2^1 \tau_7^1 (\tau_1^3 \tau_8^3 - \tau_1^3 - \tau_8^3 + I), \\
H_{21} &= -\frac{3}{2 \cdot 4^3} \tau_1^1 \tau_7^1 (-\tau_2^3 \tau_8^3 + \tau_2^3 + \tau_8^3 - I), \\
H_{23} &= -\frac{3}{2 \cdot 4^3} \tau_6^1 \tau_8^1 (-\tau_5^3 \tau_7^3 + \tau_5^3 + \tau_7^3 - I), \\
H_{24} &= -\frac{3^2}{2 \cdot 4^3} (\tau_1^1 \tau_2^1 (\tau_3^1 \tau_4^1 + \tau_7^1 \tau_8^1) + \tau_5^1 \tau_6^1 (\tau_3^1 \tau_4^1 + \tau_7^1 \tau_8^1)).
\end{aligned}$$

Appendix D: Energy convergence for the $SO(3)$ model on a 2×6 lattice

In this section, we show the energy convergence for both the ground state and the first excited state energy as a function of circuit depth (p) for the $SO(3)$ model on a 2×6 lattice, using VQE and VQD methods in Fig. 15.

Appendix E: The results for 1-d TFIM

This section collects the results of the ground and the first excited state energy for the 1-d TFIM in three different regimes for various lattice sizes using the QAOA method. To see the performance of QAOA we plot both energies and in-fidelity with the circuit depth (p) for a 1-d lattice with 10 sites in Fig. 17. In addition, we show an example of how the minimization proceeds for a given circuit depth and an initial state in Fig. 16 for several different classical optimizers (for $h_x = 0.5$ and $L = 8$) and compare among them.

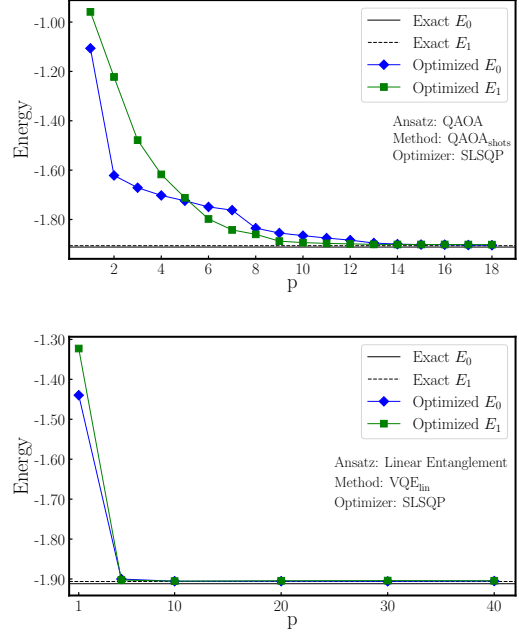


FIG. 15. (Top): The optimized ground state and first excited state energies are shown as a function of circuit depth (p) on a 2×6 lattice using the VQE algorithm (QAOA_{shots}). (Bottom): The energy convergence results are presented for the VQD method (VQE_{lin}).

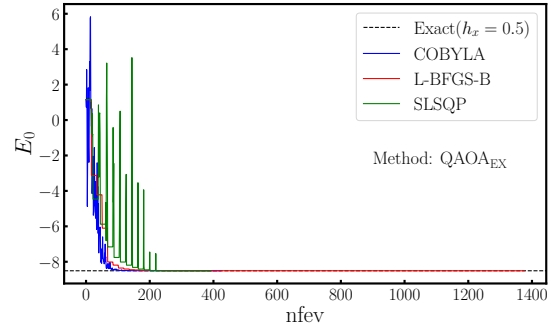


FIG. 16. Plot of the optimized ground state energy using the QAOA method (QAOA_{EX}) against the number of function evaluations for a lattice with 8 sites at $h_x = 0.5$, comparing three different optimizers. The optimizer L-BFGS-B took more iterations to converge than the others but achieved a very low in-fidelity of about 10^{-10} . In contrast, the COBYLA reached an in-fidelity of around 10^{-6} , and the SLSQP optimizer had an in-fidelity of approximately 10^{-4} .

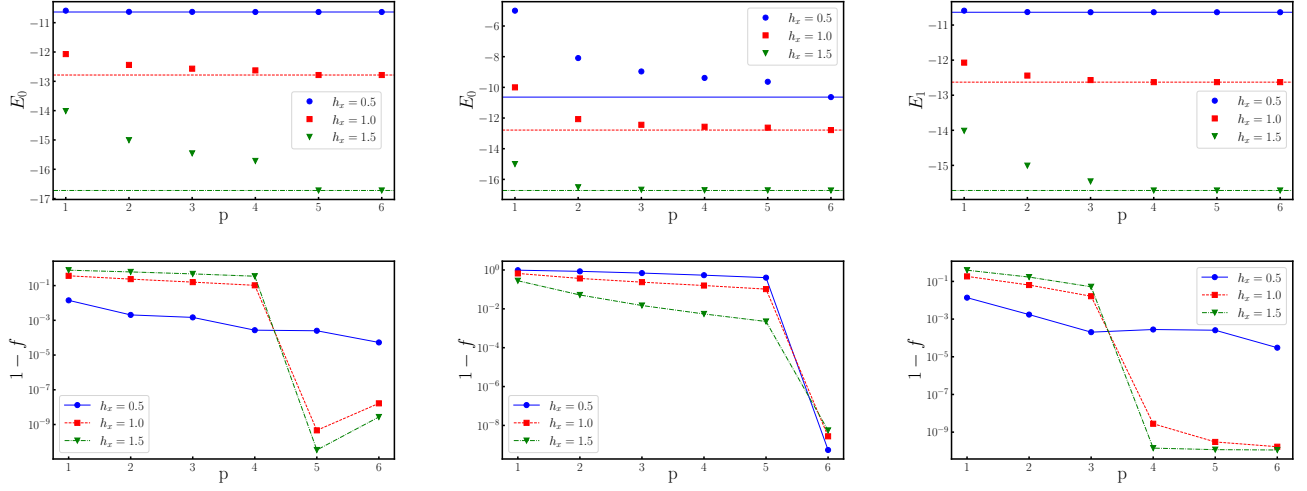


FIG. 17. (First row): We display both the ground state and the first excited state energy as a function of circuit depth (p) on a 1-d lattice with 10 sites. In the first row, the leftmost figure shows the results for the ground state with the GHZ state as an initial state, the middle figure also shows the ground state results when one starts with an eigenstate of the H_2 term as the initial state, while the rightmost figure presents the performance for the first excited state. The second row shows the corresponding in-fidelity for each of the cases in the first row.